Mitochondrial origins of the pressure to sleep

Raffaele Sarnataro[1], Cecilia D. Velasco[1], Nicholas Monaco[1], Anissa Kempf[1,2], and Gero Miesenböck[1*]

[1] Centre for Neural Circuits and Behaviour, University of Oxford, Tinsley Building, Mansfield Road, Oxford OX1 3SR, United Kingdom

[2] Present address: Biozentrum, Universität Basel, Spitalstrasse 41, CH-4056 Basel, Switzerland

[*] Correspondence: gero.miesenboeck@cncb.ox.ac.uk

Abstract

To obtain a comprehensive, unbiased view of molecular changes in the brain that may underpin the need for sleep, we have characterized the transcriptomes of single cells isolated from rested and sleep-deprived flies. Transcripts upregulated after sleep deprivation, in sleep-control neurons projecting to the dorsal fan-shaped body (dFBNs) but not ubiquitously in the brain, encode almost exclusively proteins with roles in mitochondrial respiration and ATP synthesis. These gene expression changes are accompanied by mitochondrial fragmentation, enhanced mitophagy, and an increase in the number of contacts between mitochondria and the endoplasmic reticulum, creating conduits for the replenishment of peroxidized lipids. The morphological changes are reversible after recovery sleep and blunted by the installation of an electron overflow in the respiratory chain. Inducing or preventing mitochondrial fission or fusion in dFBNs alters sleep and the electrical properties of sleep-control cells in opposite directions: hyperfused mitochondria increase, whereas fragmented mitochondria decrease, neuronal excitability and sleep. ATP levels in dFBNs rise after enforced waking because of diminished ATP consumption during the arousal-mediated inhibition of these neurons, which predisposes them to heightened oxidative stress. Consistent with this view, uncoupling electron flux from ATP synthesis relieves the pressure to sleep, while exacerbating mismatches between electron supply and ATP demand (by powering ATP synthesis with a light-driven proton pump) promotes sleep. Sleep, like ageing, may be an inescapable consequence of aerobic metabolism.

Introduction

Sleep pressure, the process variable in sleep homeostasis, has lacked a physical interpretation. Although prolonged waking is associated with numerous changes in the brain—of neuronal firing patterns[1,2], the strengths of synaptic connections[3], the organization of subcellular compartments[4-6], metabolite concentrations[7,8], and metabolic and gene expression programs[5,9,10]—, it remains generally indeterminable whether these changes are causes or consequences of a growing need for sleep. Perhaps the only opportunity for separating causation from correlation exists in specialist neurons with active roles in the induction and maintenance of sleep[11]; in these cells, sleep's proximate (and maybe also its ultimate) causes must interlock directly with the processes that regulate spiking. To delineate the molecular determinants of these processes in as complete and unbiased a manner as possible, we collected single-cell transcriptomes[12] of the brains of rested and sleep-deprived flies (Fig. S 1a). An encodable fluorescent marker allowed us to identify and enrich for two dozen sleep-inducing neurons with projections to the dorsal fan-shaped body of the central complex[13,14] (dFBNs) and compare their transcriptomic response to sleep loss with that of other identifiable cell types.

Results

Transcriptomic traces of sleep loss in mitochondria and synapses

Drosophila brains were dissociated into single-cell suspensions, and neurons expressing GFP under the control of *R23E10-GAL4*[15] were isolated by flow cytometry. We performed single-cell RNA-sequencing (10X Chromium) on cells contained in the GFP-positive and GFP-negative fractions; among the 13,173 high-quality cells retrieved (Fig. S 1b, c), neurons nominated by *R23E10-GAL4* were identified by the expression of *GFP*, the neuronal markers *embryonic lethal abnormal vision* (*elav*) and *neuronal synaptobrevin* (*nSyb*), and *Allatostatin A* (*AstA*) *receptor 1* (*AstA-R1*), whose transcriptional enhancer provides the genomic fragment driving expression in the *R23E10-GAL4* line. Most neurons within the *R23E10-GAL4* domain contained machinery for the synthesis and release of either glutamate or GABA (Fig. S 1d); some also transcribed the gene encoding the vesicular acetylcholine transporter VAChT (Fig. S 1d)—a common occurrence in non-cholinergic neurons, which rely on a microRNA to suppress its translation[16]. Indeed, fluorescent sensors detected the release of glutamate, but not of acetylcholine, from dFBNs[14].

In the *Drosophila* CNS, glutamate and GABA both act on ligand-gated chloride channels, consistent with the known inhibitory effect of dFBNs on their postsynaptic partners[14,17]. Members of the *R23E10-GAL4* pattern that expressed one or the other of these inhibitory transmitters were anatomically segregated[14]: a pair of GABAergic cells targeted the suboesophageal ganglion, while a larger glutamatergic population innervated the dFB. This latter group of *bona fide* dFBNs formed a distinct gene expression cluster of 323 cells among all glutamatergic neurons in the brain (Fig. 1a, Fig. S 1e, f). The cluster was defined by genes controlled by known dFBN enhancers (Fig. S 1g) and encoding known dFBN markers, such as the Rho GTPase-activating protein[15] crossveinless-c, the dopamine receptor[18] Dop1R2, the serotonin receptor[19] 5-HT2B, and the neuropeptide[17] AstA (Fig. 1b), but the distributions of some markers suggested further subdivisions. For example, AstA was confined to a subset of dFBNs (Fig. 1b), consistent with the comparatively mild sleep phenotype following RNA-mediated interference (RNAi) with its expression in the entire dFBN population[17].

Gene ontology analyses of the 122 transcripts whose levels in dFBNs changed after 12 h of overnight sleep deprivation pointed to only two sleep need-dependent processes: mitochondrial energy metabolism and synaptic transmission (Fig. 1c, d, Fig. S 2a–e). Sleep

loss led to the selective upregulation of transcripts encoding components of electron transport complexes I–IV, ATP synthase (complex V), the ATP/ADP carrier sesB, and enzymes of the tricarboxylic acid cycle, whereas gene products involved in synapse assembly, synaptic vesicle release, and presynaptic homeostatic plasticity[20] were selectively downregulated (Fig. 1c). Within the practical limits of our analysis, which cannot extend to every conceivable neuron type, this transcriptomic signature of sleep loss appeared unique to dFBNs: it was absent from two cell populations with comparable numerical representation in our data, namely projection neurons of the antennal lobe (PNs, 317 cells, Fig. S 3a–d) and Kenyon cells of the mushroom body (KCs, 603 cells, Fig. S 3e–h), and it was also undetectable in a combined analysis of all 12,850 non-dFBN cells (Fig. S 3i, j). There are, however, subtle hints from an independent transcriptomic study that sleep history may alter levels of mitochondrial components not only in dFBNs but also in R5 neurons of the ellipsoid body, another element of the sleep homeostat[10].

The remainder of this paper examines the causes and consequences of the differential expression of genes encoding mitochondrial proteins in dFBNs; a companion study[14] investigates the role of presynaptic plasticity in the wider context of sleep need-dependent dFBN dynamics.

A mitochondrial electron surplus induces sleep

The prominence of mitochondrial components in the transcriptional response of dFBNs to sleep deprivation (Fig. 1c, d, Fig. S 2) offers unbiased support for the hypothesis that sleep and aerobic metabolism are fundamentally connected. This hypothesis gained a firm mechanistic footing with the discovery that dFBNs regulate sleep through machinery that gears their sleep-inducing spike discharge to mitochondrial respiration[21]. The centerpiece of this mechanism is Hyperkinetic, the β-subunit of the voltage-gated potassium channel Shaker, which regulates the electrical activity of dFBNs[18,21]. Hyperkinetic is an unusual aldo-keto reductase with a stably bound nicotinamide adenine dinucleotide phosphate cofactor whose oxidation state (NADPH or $NADP^+$) reflects the fate of electrons entering the respiratory chain[21,22]. When the demands of ATP synthesis are high, the vast majority of electrons reach O_2 in an enzymatic reaction catalyzed by cytochrome *c* oxidase (complex IV); only a small minority leak prematurely from the upstream mobile carrier coenzyme Q (CoQ), producing superoxide and other reactive oxygen species[23,24] (ROS) (Fig. 2a). The probability of these non-enzymatic single-electron reductions of O_2 increases sharply under conditions that

overfill the CoQ pool as a consequence of increased supply (high $NADH/NAD^+$ ratio) or reduced demand (large protonmotive force Δp and high ATP/ADP ratio)[23,24] (Fig. 2a). The mitochondria of dFBNs appear prone to this mode of operation during waking[21], when caloric intake is high but the neurons' electrical activity is reduced, leaving their ATP reserves full. Indeed, measurements with the genetically encoded ATP sensors iATPSnFR and ATeam revealed ~1.2-fold higher ATP concentrations in dFBNs, but not PNs, after a night of sleep deprivation than at rest (Fig. 2b, c, Fig. S 4a, b). ATP levels rose acutely when dFBNs were inhibited by an arousing heat stimulus, which releases dopamine onto their dendrites[14,18] (Fig. 2a, d), and fell below baseline when dFBNs themselves were stimulated, mimicking sleep[14] (Fig. 2a, e).

Even if the chance of an individual electron spilling from the CoQ pool is low, however, metabolically highly active cells, such as neurons, will by the sheer number of electrons passing through their respiratory chains generate significant amounts of ROS[23-25]. Their anti-cyclical relationship between energy availability (which peaks during waking) and energy consumption (which in a sleep-active neuron peaks during sleep) may thus predispose dFBNs to an exaggerated form of the electron leak experienced by many neurons in the awake state, making them an effective early warning system against widespread damage. As polyunsaturated membrane lipids appear especially at risk, dFBNs estimate the size of the mitochondrial electron leak indirectly, by counting reductions of lipid peroxidation-derived carbonyls at Hyperkinetic's active site[22].

Several lines of evidence point to a mismatch between the number of electrons entering the mitochondrial transport chain and the number needed to fuel ATP production as a root cause of sleep. First, opening an exit route for surplus electrons from the CoQ pool (by equipping the mitochondria of dFBNs with the alternative oxidase[26] (AOX) of *Ciona intestinalis*, which produces water in a controlled four-electron reduction of O_2) relieved not only the basal pressure to sleep[21] but also remedied the excessive sleep need of flies whose ability to remove breakdown products of peroxidized lipids was impaired[22]. Second, increasing the demand of dFBNs for electrons (by overexpressing the uncoupling proteins Ucp4A or Ucp4C, which short-circuit the proton electrochemical gradient across the inner mitochondrial membrane[27], Fig. 2a) decreased sleep (Fig. 2f, Fig. S 4c). And third, powering ATP synthesis with photons rather than electrons (by illuminating a mitochondrially targeted

version of the light-driven archaeal proton pump delta-rhodopsin[28], Fig. 2a, Fig. S 4d) made NADH-derived electrons in dFBNs redundant and precipitated sleep (Fig. 2g, h, Fig. S 4e, f).

Sleep alters mitochondrial dynamics

Given this wealth of evidence, it is not surprising that mitochondria would emerge as one of two pivots in the reorganization of dFBN gene expression after sleep deprivation (Fig. 1c, d, Fig. S 2). However, it remains ambiguous whether the upregulation of transcripts encoding mitochondrial proteins signals a net increase in mitochondrial mass or a compensatory response to organelle damage. To disambiguate these scenarios, we labelled the mitochondria of dFBNs with matrix-localized GFP (mito-GFP) and, in independent series of experiments, imaged the neurons' dendritic fields by confocal point-scan or optical photon reassignment microscopy[29] (CLSM or OPRM, respectively). Both forms of light microscopy were validated against ultrastructure: automated morphometry of deconvolved image stacks established that, although either optical method overestimated the true organelle size to a different extent, the size ratios of mitochondria in dFBNs and uniglomerular olfactory PNs of the antennal lobes matched that determined by volume electron microscopy[30] (Fig. S 5a, b). While diffraction undoubtedly inflated the absolute dimensions of mitochondria, especially in CLSM images, valid inferences about relative morphological differences could therefore still be drawn.

A night of sleep loss, regardless of whether caused by mechanical agitation or an artificial elevation of arousing dopamine[18], reduced the size, elongation, and branching of dFBN mitochondria (Fig. 3a, b, Fig. S 5c–f), and it led to the relocation of dynamin-related protein 1 (Drp1), the key fission dynamin of the outer membrane[31-33], from the cytosol to the mitochondrial surface (Fig. 3c). OPRM, which achieves lateral super-resolution ~2-fold above the diffraction limit[29], detected a concomitant increase in mitochondrial number (Fig. 3b), indicative of organelle division, which eluded CLSM (Fig. S 5f, but see Methods for a cautionary remark about the interpretation of absolute mitochondrial numbers). This incomplete tally of daughter mitochondria notwithstanding, the two methods painted congruous pictures of mitochondrial fission after sleep loss (Fig. 3a, b, Fig. S 5c–f). The mitochondria of antennal lobe PNs, in contrast, bore no vestiges of sleep history (Fig. S 6).

AOX protected dFBN mitochondria against sleep loss-induced fragmentation (Fig. 3b, Fig. S 5e–g), underlining that ROS generation during waking[21] is the initial spark that triggers

fission[24,34]. In the same vein, depolarization of dFBNs during mechanical sleep deprivation, which increases ATP consumption by the Na^+/K^+ pump and thereby reduces the diversion of electrons into ROS (Fig. 2a), preserved the morphology of their mitochondria (Fig. 3b, Fig. S 5e–g).

Mitochondrial fission is a prelude to the proliferation of mitochondria at contact sites with the endoplasmic reticulum[35] (ER) and/or the shedding and clearance of dysfunctional organelle fragments by mitophagy[36] (Fig. 3c). Sleep deprivation stimulated both processes: the reconstitution of fluorescence from GFP fragments anchored in the outer mitochondrial and ER membranes ($SPLICS_{short}$, whose mere presence had no impact on sleep (Fig. S 5h)) revealed a higher contact site count in dFBNs of sleep-deprived flies (Fig. 3d), whereas mito-QC, a ratiometric sensor detecting the entry of mitochondria into acidic autophagolysosomes, reported enhanced mitophagy (Fig. 3e). Mitochondria–ER contacts (MERCS) concentrate the fission and fusion machineries[35,37] whose dynamic equilibrium determines the steady-state morphology of the mitochondrial network and support mitochondrial biogenesis by allowing the passage of phospholipids from the ER[38,39]. The abundance of MERCS in sleep-deprived dFBNs (Fig. 3d) may thus not only echo a recent wave of mitochondrial fission (Fig. 3a, b, Fig. S 5c–f) but also prefigure, as we suspect the abundance of transcripts for mitochondrial proteins does (Fig. 1c), the proliferation and fusion of mitochondria during subsequent recovery sleep, which caused their volume, shape, and branch length to rebound above baseline values (Fig. 3a, b, Fig. S 5e, f).

Mitochondrial dynamics alter sleep

If shifts in the balance between mitochondrial fission and fusion are part of a feedback mechanism which corrects mismatches between NADH supply and ATP demand[24,40,41] that cause sleep pressure to rise or fall, then the experimental induction of these homeostatic responses in dFBNs should move the set points for sleep: mitochondrial fragmentation is predicted to decrease, and mitochondrial fusion is predicted to increase, sleep duration and depth. To test these predictions, we took experimental control of the three GTPases with central regulatory roles in mitochondrial dynamics (Fig. 4a, Fig. S 7a–c): the fission dynamin Drp1[31-33], and integral proteins of the inner and outer mitochondrial membranes, termed optic atrophy 1 (Opa1) and mitofusin or mitochondrial assembly regulatory factor (Marf), respectively, whose oligomerization in *cis* and *trans* fuses the corresponding membranes[32,42-44]. As in our manipulations of mitochondrial protonmotive force (Fig. 2f–h,

Fig. S 4c–f), *R23E10-GAL4* and the intersectional driver *R23E10* ∩ *VGlut-GAL4*, which targets only *bona fide* glutamatergic dFBNs of the central brain[14] (Fig. 1a), were used interchangeably in these experiments (Fig. 4, Fig. S 8).

Fragmenting dFBN mitochondria through the overexpression of Drp1 or the RNAi-mediated depletion of Opa1—and, to a lesser extent, of Marf—decreased sleep (Fig. 4b, c, Fig. S 8a–e), abolished the homeostatic response to sleep deprivation (Fig. 4d, Fig. S 8f), and reduced ATP levels in dFBNs regardless of sleep history (Fig. S 7d). Tipping the equilibrium toward mitochondrial fusion had the opposite effect: dFBN-restricted knockdown of Drp1 or the overexpression of Opa1 plus Marf—or of Opa1 alone, but not of Marf alone—increased baseline as well as rebound sleep (Fig. 4b–d, Fig. S 8a, f, g) and elevated the arousal threshold (Fig. S 9a, b) without causing overexpression artefacts or overt developmental defects (Fig. S 9c, d). None of these interventions altered sleep when targeted to PNs or KCs (Fig. S 10). The indiscriminate sleep losses reported[6] after pan-neuronal or glial RNAi knockdowns of either Drp1 or Marf—which in dFBNs alter sleep bidirectionally (Fig. 4b–d, Fig. S 8a, f), reflecting their antagonistic mitochondria-shaping roles—are difficult to interpret without parallel measurements of mitochondrial (and possibly peroxisomal) form and function. Taken at face value, they could hint that the fusion–fission cycles of many non-dFBN cells are not tied to the sleep–wake cycle but operate continuously to mix and re-compartmentalize mitochondrial content for maintenance or metabolic control[40,41].

In dFBNs, the large and opposite behavioral consequences of promoting mitochondrial fission or fusion (Fig. 4b–d) went hand-in-hand with established biophysical signatures of low or high sleep pressure[15]. dFBNs in short sleepers overexpressing Drp1 had shallower current–spike frequency functions than neurons in control animals, whereas the converse was true in somnolent overexpressers of Opa1 and Marf (Fig. 4e–g), whose dFBNs generated an elevated number of somnogenic bursts[14] as part of their enhanced responses (Fig. 4e, h).

A striking feature of sleep-deprived brains is the depletion of phosphatidic acid[22] (PA), a fusogenic[45] glycerophospholipid. Mitochondrial PA is a cleavage product of cardiolipin, generated by a local phospholipase D (mitoPLD)[45] (Fig. 4a). Underlining the importance of PA for the fusion reaction, and of mitochondrial fusion for the regulation of sleep, *R23E10* ∩ *VGlut*- or *R23E10-GAL4*-restricted interference with the expression of the mitoPLD zucchini or the outer membrane protein Mitoguardin (Miga), which stabilizes catalytically active

mitoPLD[46] and/or transfers phospholipids (including PA) from other cellular membranes to mitochondria[47,48], recapitulated the sleep losses seen when the protein-based fusion machinery of these neurons was targeted by RNAi or antagonized by the overexpression of Drp1 (Fig. 4c, Fig. S 8b).

Discussion

Aerobic metabolism was the innovation that, following the first of two large increases in atmospheric O_2 levels 2.4 billion and 750–570 million years ago, allowed eukaryotes to maximize the free energy yield of electron transfers, setting the stage for the Cambrian explosion of multicellular life in the wake of the second O_2 revolution[49]. Power-hungry nervous systems appeared[50]—and with them, apparently, the need for sleep[51]. Although sleep is likely since to have acquired additional functions, such as synaptic homeostasis or memory consolidation[3], an empirical power law[52] that relates daily sleep amount to mass-specific O_2 consumption[53] suggests that sleep serves an ancient metabolic purpose also in mammals. The allometric exponent in this power law is a multiple of $\frac{1}{4}$ rather than the $\frac{1}{3}$ expected from Euclidean geometric scaling—a sign that the distribution of resources by centralized networks, such as the vascular and respiratory systems, is responsible[52,54]. Thanks to higher terminal branch densities, these networks allocate more O_2 to each cell in small animals, allowing their metabolism to run 'hotter' than that of large mammals, whose cells are supply-limited[54]. The price to pay is a shorter life, a greater fraction of which is spent asleep.

If sleep indeed evolved to fulfill a metabolic need, it is not surprising that neurons controlling sleep and energy balance would be regulated by similar mechanisms. In the mammalian hypothalamus, the mitochondria of orexigenic neurons expressing agouti-related protein (AgRP) and of anorexigenic neurons expressing pro-opiomelanocortin undergo antiphasic cycles of fission and fusion[55]. These cycles are coupled to changes in the energy balance of mice[55], just as cycles of mitochondrial fission and fusion in dFBNs are coupled to changes in the sleep balance of flies. The electrical output of AgRP neurons increases after mitochondrial fusion to promote weight gain and fat deposition[55], just as the electrical output of dFBNs increases after mitochondrial fusion to promote sleep. Deletions of mitofusins from AgRP neurons impair the consumption of food[55], just as interference with mitochondrial fusion in dFBNs impairs the induction of sleep. These parallels suggest that sleep pressure and hunger both have mitochondrial origins, and that electrons flow through the respiratory chains of the respective feedback controllers like sand in the hourglass that determines when balance must be restored.

Methods

***Drosophila* strains and culture.** Flies were grown on media of cornmeal (62.5 g l^{-1}), inactive yeast powder (25 g l^{-1}), agar (6.75 g l^{-1}), molasses (37.5 ml l^{-1}), propionic acid (4.2 ml l^{-1}), tegosept (1.4 g l^{-1}), and ethanol (7 ml l^{-1}) under a 12 h light:12 h dark cycle at 25 °C in ~60% relative humidity, unless stated otherwise. To prevent the undesired activation of optogenetic actuators or the photoconversion of all-*trans* retinal by ambient light, flies expressing CsChrimson or mito-dR and their controls were reared and housed in constant darkness and transferred to food supplemented with 2 mM *all-trans* retinal (Molekula) in DMSO, or to DMSO vehicle only, 2 days before the optical stimulation experiments, at an age of 1–2 days post eclosion. Flies expressing TrpA1 and their controls were cultured and maintained at 21 °C and shifted to 29 °C for 12 h.

Transgene expression was directed to dFBNs by driver lines *R23E10-GAL4*[56] or *R23E10* ∩ *VGlut-GAL4*[14] (created by reconstituting GAL4 from hemidrivers[57] *R23E10-DBD*[58] and *VGlut-p65AD*[59]); PNs, KCs, and dopaminergic neurons were targeted by *GH146-GAL4*[60], *OK107-GAL4*[61], and *TH-LexA*[62], respectively. Effector transgenes encoded fluorescent markers for flow cytometry (*UAS-6xEGFP*[63]), visually guided patch-clamp recordings (*UAS-mCD8::GFP*[64]), mitochondrial morphometry (*UAS-mito-GFP*[65,66]), or ratiometric imaging (*UAS-RFP* or *UAS-tdTomato*); integral proteins of the outer mitochondrial membrane[67] (*UAS-OMM-mCherry*), endoplasmic reticulum[68] (*UAS-tdTomato-Sec61β*), or plasma membrane[69] (*UAS-CD4-tdTomato*); the ATP sensors iATPSnFR$^{1.0}$ (refs. [70,71]) or ATeam1.03NL (refs. [72,73]); the mitochondrial alternative oxidase AOX of *Ciona intestinalis*[74]; delta-rhodopsin of *Haloterrigena turkmenica* with an inner mitochondrial membrane-targeting sequence[28,75] (mito-dR); the opto- or thermogenetic actuators[76] CsChrimson[77] or TrpA1 (the latter in *UAS*- and *lexAop*-driven versions[78,79]); the mitochondria–ER contact site[80,81] or mitophagy[82,83] reporters SPLICS$_{short}$ or mito-QC; overexpression constructs encoding Ucp4A or Ucp4C[84,85], Drp1 (3 independent transgenes[86-88]), Opa1[87], or Marf (2 independent transgenes[87,89]); or RNAi transgenes for interference with the expression of *Drp1*[89], *Opa1* (7 independent transgenes[86,90,91]), *Marf* (5 independent transgenes[86,90,91]), *zucchini*[91], or *Mitoguardin* (2 independent transgenes[90]). Recombinant strains carrying the *UAS-Marf* and *R23E10-GAL4* or *R23E10-DBD* transgenes on the third chromosome were generated to enable the co-expression of Opa1 and Marf. Endogenous Drp1 was colocalized with mitochondria in *Drp1::FLAG-FlAsH-HA* flies[92].

Sleep measurements, sleep deprivation, and sleep induction by photoenergized mitochondria. In standard sleep assays, females aged 2–4 days were individually inserted into 65-mm glass tubes containing food reservoirs, loaded into the Trikinetics *Drosophila* Activity Monitor system, and housed under 12 h light:12 h dark conditions at 25 °C in 60% relative humidity. Flies were allowed to habituate for one day before sleep—classified as periods of inactivity lasting >5 minutes[93,94] (Sleep and Circadian Analysis MATLAB Program[95])—was averaged over two consecutive recording days. Immobile flies (< 2 beam breaks per 24 h) were manually excluded.

Our standard method of sleep deprivation used the sleep-nullifying apparatus[96] (SNAP): a spring-loaded platform stacked with Trikinetics monitors was slowly tilted by an electric motor, released, and allowed to snap back to its original position. The mechanical cycles lasted 10 s and were repeated continuously for 12 h, beginning at zeitgeber time 12. Flies expressing TrpA1 in dFBNs (and relevant controls) were mechanically sleep-deprived at 29 ˚C.

To guard against side effects of regular mechanical agitation, we explored two alternative methods of sleep deprivation, with comparable results. In some behavioral experiments (Fig. S 8f), an Ohaus Vortex Mixer stacked with Trikinetics monitors produced horizontal circular motion stimuli with a radius of ~1 cm at 25 Hz for 2 s; in contrast to the rhythmic displacement of flies in the sleep-nullifying apparatus[96], stimulation periods were randomly normally distributed within 20-s bins, hindering adaptation. And in some morphometric experiments, flies expressed TrpA1 in arousing dopaminergic neurons[18], whose activation at 29 ˚C produced sleep deprivation without sensory stimulation (Fig. S 5c, d).

Rebound sleep was measured in the 24-h window after deprivation. A cumulative sleep loss plot was calculated for each individual by comparing the percentage of sleep lost during overnight sleep deprivation to the immediately preceding unperturbed night. Individual sleep regained was quantified by normalizing the difference in sleep amount between the rebound and baseline days to baseline sleep. Only flies losing >95% of baseline sleep were included in the analysis.

Arousal thresholds were determined by applying horizontal circular motion stimuli with a radius of ~1 cm at 8 Hz, generated by a Talboys Multi-Tube Vortexer. Stimuli lasting 0.5 to 20 s were delivered once every hour between zeitgeber times 0 and 24, and the percentages of sleeping flies (if any) awakened within 1 minute of each stimulation episode were quantified.

For experiments with photoenergized mitochondria[28,75], 3–5 day old females expressing *R23E10* ∩ *VGlut-GAL4*- or *R23E10-GAL4*-driven mito-dR and their parental controls were reared for 2 days on standard food supplemented with all-*trans* retinal (or DMSO vehicle only, as indicated) and individually transferred into the wells of a flat-bottom 96-well plate. Each well contained 150 µl sucrose food (5% sucrose, 1% agar) with or without 2 mM all-*trans* retinal. The plate was sealed with a perforated transparent lid, inserted into a Zantiks MWP Z2S unit operated at 25 °C, and illuminated from below by infrared LEDs while a camera captured 31.25 frames s^{-1} from above. Zantiks software extracted time series of individual movements, which were converted to sleep measurements with the help of a custom MATLAB script detecting continuous stretches of zero-speed bins lasting >5 minutes. After flies had been allowed to habituate for at least one day in the absence of stimulation light, high-power LEDs running on an 80% duty cycle at 2 Hz (PWM ZK-PP2K) delivered ~7 mW cm^{-2} of 530-nm light for 1 h. Movement was monitored for 24 h, including the initial hour of optogenetic stimulation. If flies were found dead at the end of the experiment, data from the 1-hour time bin preceding the onset of continuous immobility (>98% zero-speed bins during ≥2 consecutive hours until the end of the recording) onward were excluded. The >98% threshold was applied to avoid scoring rare instances of video tracker noise as movement.

Brain dissociation and cell collection for single-cell RNA-sequencing. On each experimental day, averages of 186 rested and 144 sleep-deprived female flies were retrieved alive from Trikinetics monitors (Extended Data Fig, 1a) and dissected in parallel in ice-cold Ca^{2+}- and Mg^{2+}-free Dulbecco's PBS (Thermo Fisher) supplemented with 50 µM D(-)-2-amino-5-phosphonovaleric acid, 20 µM 6,7-dinitroquinoxaline-2,3-dione, and 100 nM tetrodotoxin (tDPBS) to block excitatory glutamate receptors and voltage-gated sodium channels. The lower number of sleep-deprived flies recovered reflects mortality associated with the operation of the sleep-nullifying aparatus. Brains were transferred to Protein LoBind microcentrifuge tubes containing ice-cold Schneider's medium supplemented with the same toxins (tSM), washed once with 1 ml tSM, incubated in tSM containing 1.11 mg ml^{-1} papain

and 1.11 mg ml^{-1} collagenase I for 30 minutes at room temperature, washed again with tSM, and subsequently triturated with flame-rounded 200 µl pipette tips. Dissociated brain cells were collected by low-speed centrifugation (2,000 rpm, 3 minutes), resuspended in 1 ml tDPBS, and filtered through a 20 µm CellTrics strainer. For the isolation of cells by flow cytometry (FACS), dead cells were excluded with the help of a DAPI viability dye (1 µg ml^{-1}, BD Pharmingen). Single cells were gated for based on forward and side scatter parameters, followed by subsequent gating for EGFP-negative cells, using FACSDiva software (Becton Dickenson). Both the EGFP-positive fraction and the EGFP-negative flow-through were collected for sequencing. Samples were partitioned into single cells and barcoded using droplet microfluidics[12] (10X Chromium v3 and v3.1) and multiplexed during Illumina NovaSeq6000 sequencing. Brains and dissociated cells were kept on ice or at ice-cold temperatures from dissection to sample submission, including during the FACS sorting procedure, but not during the enzymatic and mechanical dissociation steps, which took place at room temperature.

scRNA-seq data processing and alignment. Raw transcriptomic data were pre-processed with a custom command line script[12,97,98], which extracted cell barcodes and aligned associated reads to a combination of the *Drosophila melanogaster* genome release BDGP6.22 and the reference sequences of the *GAL4* and *EGFP-p10*$^{3'UTR}$ transgenes, using STAR with default settings. Flybase version FB2018_03 gene names were used for annotation. The cumulative fraction of reads as a function of cell barcodes, arranged in descending order of the number of reads, was inspected, and only cells with a high number of reads, up to a clearly visible shoulder, were retained[12]; beads with few reads, potentially ambient RNA, were discarded. All subsequent analyses were performed in R, using the Seurat v4.1 package[99].

Three biological replicates, collected on different days from independent genetic crosses, were merged, variation driven by individual batches was regressed out, and the data were normalized by dividing by the number of unique molecular identifiers (UMIs) per cell and multiplying by 10,000. Applying standard criteria for fly neurons[10,98,100,101], we rejected genes detected in fewer than 3 cells and retained only cells associated with 800–10,000 UMIs and 200–5,000 transcripts.

Principal component analysis was used to compress the expression data from an initial dimensionality of 10,000 (the number of variable features) to 50 (the number of principal components we chose to consider); the scores along these 50 dimensions were then visualized in a two-dimensional uniform manifold approximation and projection (UMAP) embedding. Clusters were identified by constructing a shared nearest neighbour graph and applying the Louvain algorithm with resolution 0.2. Clusters were manually annotated according to the presence of established markers[98,100]: Cholinergic, glutamatergic, and GABAergic neurons expressed *embryonic lethal abnormal vision* (*elav*) and *neuronal synaptobrevin* (*nSyb*) and, respectively, genes encoding the vesicular acetylcholine (VAChT) or glutamate transporters (VGlut) or glutamic acid decarboxylase 1 (Gad1) at levels >2; KCs were identified by the expression of *eyeless* and *Dop1R2* and partitioned into αβ, α'β', and γ divisions according to the distributions of sNPF, fasciclin 2, and trio; monoaminergic neurons were identified by the presence of the vesicular monoamine transporter Vmat and divided into dopaminergic, serotonergic, and octopaminergic/tyraminergic neurons by the coexpression of genes for biosynthetic enzymes (Dopa decarboxylase, tyrosine hydroxylase, tyrosine decarboxylase 2 (Tdc2), tryptophan hydroxylase, and tyramine β-hydroxylase) and vesicular transporters for dopamine or serotonin (DAT and SerT); PNs were defined and classified by the expression of the transcription factors cut and abnormal chemosensory jump 6 (acj6), with or without Lim1; glia lacked elav and nSyb but expressed the Na^+/K^+ ATPase encoded by the *nervana 2* gene, while astrocytes also contained the astrocytic leucine-rich repeat molecule (alrm); cells of the fat body were recognized by the expression of *Secreted protein, acidic, cysteine-rich* (*SPARC*), *Metallothionein A* (*MtnA*), *I'm not dead yet* (*Indy*), and *pudgy*; *R23E10* neurons expressed *elav* and *nSyb* plus *AstAR-1* and *EGFP* at a level >2. Expression level cutoffs for *VAChT*, *VGlut*, *Gad1*, and *EGFP* were chosen to bisect bimodal distributions (Fig. S 1d). For re-clustering neurons expressing specific fast-acting neurotransmitters, dFBNs, KCs, or PNs, 150 genes were used as variable features.

Differential gene expression and gene ontology analyses. Differentially expressed genes were identified in Seurat via the 'FindMarkers' function, using the 'RNA assay' counts of the two comparison groups, and restricted to genes detected in ≥1% of cells in either of the two groups with, on average, a ≥0.01-fold (log scale) expression level difference between the rested and sleep-deprived states. Expression levels were compared by Bonferroni-corrected Wilcoxon rank-sum test.

Gene ontology terms enriched in the set of differentially expressed nuclear genes were identified using PANTHER v17 or the ViSEAGO 1.4.0 and topGO 2.42.0 packages. PANTHER compared the list of differentially expressed genes to the *Drosophila melanogaster* reference list and the GO annotation database (doi: 10.5281/zenodo.7942786, version 2023-05-10). In ViSEAGO and topGO, differentially expressed genes were compared to a reference set of all variable genes used in Seurat and annotated in Ensembl; only GO terms with more than 40 attached genes were considered, and enriched terms with unadjusted $P < 0.001$ were clustered hierarchically according to Wang's distance[102].

Two-photon imaging. Females aged 3–4 days were head-fixed to a custom mount with eicosane (Sigma) and imaged on Movable Objective Microscopes with galvanometric or resonant scanners (MOM, Sutter Instruments) controlled through ScanImage software (Vidrio Technologies). Cuticle, adipose tissue, and trachea were removed to create an optical window, and the brain was superfused with carbogenated extracellular solution (95% O_2 – 5% CO_2, pH 7.3, 275 mOsm) containing (in mM) 103 NaCl, 3 KCl, 5 TES, 8 trehalose, 10 glucose, 7 sucrose, 26 $NaHCO_3$, 1 NaH_2PO_4, 1.5 $CaCl_2$, 4 $MgCl_2$. To excite iATPSnFR and co-expressed tdTomato, Mai Tai DeepSee (Spectra Physics model eHP DS) or Coherent Chameleon Ultra II Ti:sapphire lasers produced 930-nm excitation light pulses whose power was modulated by Pockels cells (302RM, Conoptics). Emitted photons were collected by 20×/1.0 NA water immersion objectives (W-Plan-Apochromat, Zeiss), split into green and red channels by dichromatic mirrors (Chroma 565dcxr or Semrock BrightLine 565nm), and detected by GaAsP photomultiplier tubes (H10770PA-40 SEL, Hamamatsu Photonics). The emission paths contained bandpass filters for iATPSnFR (Semrock BrightLine FF01-520/60) and tdTomato (Chroma ET605/70m), respectively. Photocurrents were passed through high-speed amplifiers (HCA-4M-500K-C, Laser Components) and integrators (BLP-21.4+, Mini-Circuits, or EF506, Thorlabs) to maximize the signal-to-noise ratio.

To open the conductance of CsChrimson, a 625-nm LED (M625L3, ThorLabs) controlled by a dimmable LED driver (ThorLabs) delivered 0.5–25 mW cm^{-2} of optical power through a bandpass filter (Semrock BrightLine FF01-647/57-25) to the head of the fly. Stimulus trains lasted for 2 minutes and consisted of ten 25-ms light pulses in 500-ms bursts recurring once per s. To apply arousing heat, an 808-nm laser diode (Thorlabs L808P500MM) was mounted on a temperature-controlled heat sink (ThorLabs TCDLM9 with ThorLabs TED200C controller) and aimed at the abdomen of the fly. The diode was restricted to a maximal output

of 50 mW by a ThorLabs LDC210C laser diode controller, and 2-s pulses were delivered every 30 s for 2 minutes. Images of 256 × 256 pixels were acquired at a rate of 29.13 Hz. The voltage steps controlling the LED or laser diode were recorded in a separate imaging channel for post-hoc alignment.

To drive proton pumping by mito-dR, a 530-nm LED (M530L3, ThorLabs) controlled by a dimmable LED driver (ThorLabs) delivered ~25 mW cm^{-2} of optical power through an ACP2520-A collimating lens (ThorLabs) to the head of the fly. Stimuli lasted for 400 ms and were repeated every 10 s. Two shutters, one in the combined fluorescence emission path (Ø1/2" stainless steel diaphragm optical beam shutter with controller, Thorlabs) and one on the LED (Vincent/UniBlitz VS35S2ZM1R1-21 Uni-Stable Shutter with UniBlitz VMM-T1 Shutter Driver/Timer Controller), opened alternately during imaging and green light stimulation. Images of 128 × 50 pixels were acquired at a rate of 41.59 Hz. The voltage steps controlling the LED were recorded in a separate imaging channel for post-hoc alignment.

Time series of average fluorescence in manually selected dendritic regions of interest (ROIs) were analysed in MATLAB, following the subtraction of a time-varying background. ΔF/F curves were calculated separately for each trial as $\Delta F_t/F_0 = (F_t - F_0)/F_0$, where F_0 is the mean fluorescence intensity before stimulation onset (170 s for heat and CsChrimson, 4 s for mito-dR) and F_t is the fluorescence intensity in frame t; $\Delta R_t/R_0$ represents the iATPSnFR/tdTomato (green-red) intensity ratio. The stimulus-aligned $\Delta R_t/R_0$ signals were averaged across two trials in the case of CsChrimson and 30 trials in the case of mito-dR and then across flies; the statistical units are flies. For display purposes, traces were smoothed with moving-average filters (15-s windows for heat and CsChrimson, followed by down-sampling by a factor of 100; 1-s window for mito-dR).

Super-resolution and confocal imaging. Single-housed females aged 6 days post eclosion were dissected at zeitgeber time 0, following *ad libitum* sleep or 12 h of sleep deprivation. Experimental and control samples were processed in parallel. Brains were fixed for 20 min in 0.3% (v/v) Triton X-100 in PBS (PBST) with 4% (w/v) paraformaldehyde, washed five times with PBST, incubated with primary antibodies and secondary detection reagents where indicated, mounted in Vectashield, and imaged. Only anatomically intact specimens from live flies (at the point of dissection) were analysed, blind to sleep history, using existing, adapted, or newly developed (semi-)automated routines in Fiji.

For mitochondrial morphometry[103], z-stacks of the dendritic fields of mito-GFP-expressing dFBNs (or the glomerular arborizations of PNs) were collected at the Nyquist limit, with identical image acquisition settings across all conditions. Dendrites were chosen as an optically favourable compartment for analysis because their branches (and the mitochondria within them) were well separated along all axes.

Optical photon reassignment (OPRM) super-resolution images were collected on an Olympus IX83 P2ZF microscope equipped with a UplanSApo 60×/1.30 NA silicon oil objective and a Yokogawa CSU-W1 super-resolution by optical pixel reassignment (SoRa) spinning-disk module[29]. Image stacks were passed through a 'low' Olympus Super Resolution spatial frequency filter and deconvolved in five iterations of a constrained maximum likelihood algorithm (Olympus cellSens).

Confocal laser-scanning (CLSM) images were acquired on a Leica TCS SP5 confocal microscope with an HCX IRAPO L 25×/0.95 NA water immersion objective. Point-spread functions were created with the PSF Generator plugin[104] in Fiji and used to deconvolve the images with DeconvolutionLab2 software[105,106] employing the Richardson-Lucy TV algorithm with regularization set to 0.0001 and a maximum of two iterations[103].

Functions of the Mitochondria Analyser plugin in Fiji were applied in an automated fashion to the deconvolved OPRM and CLSM images to remove background noise ('subtract background' with a radius of 1.25 µm), reduce noise and smooth objects while preserving edges ('sigma filter plus'), enhance dim areas while minimizing noise amplification ('enhance local contrast' with slope 1.4), and optimize the use of image bits ('gamma correction' with a value of 0.90) before thresholding ('weighted mean' with block size 1.25 µm and a C value of 5 for dFBNs and 12 for PNs, determined empirically to minimize background noise[103]). The resulting binary images were examined via Batch 3D analysis on a 'per-cell' basis to extract morphological metrics; OPRM image stacks were rendered in three dimensions with the 'Volume Viewer' plugin in Fiji, using trilinear interpolation in volume mode with default settings and a grayscale transfer function. The full dendritic fields of dFBNs were analysed, but the high packing density of PN dendrites in the glomeruli of the antennal lobe forced us to select 20 substacks per glomerulus, each with an axial depth of 6 µm (for OPRM) or 5.8 µm (for CLSM), using a Fiji random number generator function, to

make computations practical. Morphometric parameters were then averaged across all substacks per glomerulus.

When other *UAS*-driven transgenes were present in addition to *UAS-mito-GFP*, the dilution of a limiting amount of GAL4 among multiple promoters led to a noticeable dimming of mitochondrial fluorescence, especially in OPRM images. We therefore sought to compare mitochondrial morphologies within (Fig. 3a, b, Fig. S 5g, Fig. S 6a, b) or among (Fig. S 5c, d, Fig. S 7a, b) genotypes carrying the same number of *UAS*-driven transgenes. While shape metrics, such as the mean volume, sphericity, and branch length of mitochondria, appeared robust under variations in brightness, the number of fluorescent objects crossing the detection threshold was not. Because the absolute number of mitochondria within an image stack also depends on the volume fraction occupied by dFBN dendrites, these confounds should be borne in mind when interpreting mitochondrial counts.

For ratiometric snapshot imaging of the ATP sensors iATPSnFR (normalized to co-expressed RFP) and ATeam and the mitophagy sensor mito-QC, fluorescence was quantified on summed z-stacks of the relevant channels, following the subtraction of average background in manually defined areas close to the structures of interest. Brains expressing ATeam were imaged on a Zeiss LSM980 with Airyscan2 microscope with a Plan-Apochromat 40×/1.3 NA oil immersion objective, an excitation wavelength of 445 nm for the FRET donor mCFP, and emission bands of 454–507 nm for CFP and 516–693 nm for the YFP variant mVenus[73]. In ATP calibration experiments (see below), the biocytin-filled dFBN soma was identified after staining with Alexa Fluor 633 streptavidin (ThermoFisher, 1:600 in 0.3% PBST at 4 ˚C overnight) at excitation and emission wavelengths of 639 nm and 649–693 nm, respectively. Images of iATPSnFR plus RFP and mito-QC were acquired on a Leica TCS SP5 confocal microscope with HCX IRAPO L 25×/0.95 NA water and HCX PL APO 40×/1.30 NA oil immersion objectives, respectively. The excitation and emission wavelengths were 488 nm and 498–544 nm for iATPSnFR, 555 nm and 565–663 nm for RFP, and 488 nm and 503–538 nm, and 587 nm and 605–650 nm, for the GFP and mCherry moieties of mito-QC, respectively.

To convert the emission ratios of ATeam1.03NL into approximate ATP concentrations, we constructed a calibration curve *in vivo* by including 0.15, 1.5, or 4 mM MgATP, along with 10 mM biocytin, in the intracellular solution during whole-cell patch-clamp recordings. After

dialyzing the recorded dFBN for 30 minutes, the patch electrode was withdrawn, and the brain was recovered, fixed, and processed for detection and ratiometric imaging of the biocytin-labelled soma. A standard curve was obtained by fitting the Hill equation, with a dissociation constant[73] of 1.75 mM and a Hill coefficient[72] of 2.1, to the YFP-CFP fluorescence ratios of dFBN somata containing known ATP concentrations.

SPLICS puncta[80,107] were imaged on a Leica TCS SP5 confocal microscope with an HCX PL APO 40×/1.30 NA oil immersion objective, excitation and emission wavelengths of 488 nm and 500–540 nm, respectively, and analysed in Fiji with a custom macro based on the existing 'Quantification 1 and 2' plugins[107]. Only puncta exceeding 10 voxels were counted.

For localizing Drp1, we labelled the mitochondria of dFBNs with mito-GFP in *Drp1::FLAG-FlAsH-HA* flies[92], whose genomic *Drp1* coding sequence is fused in frame with a FLAG-FlAsH-HA tag. Fixed brains were incubated sequentially at 4 °C in blocking solution (10% goat serum in 0.3% PBST) overnight, with mouse monoclonal anti-FLAG antibody (anti-DDK; 1:1,000, OriGene) in blocking solution for 2–3 days, and with goat anti-Mouse Alexa Fluor 633 (1:500, ThermoFisher) in blocking solution for two days. The samples were washed five times with PBST before and after the addition of secondary antibodies, mounted, and imaged on a Leica TCS SP5 confocal microscope with an HCX PL APO 40×/1.30 NA oil immersion objective. The excitation and emission wavelengths were 488 nm and 500–540 nm for mito-GFP and 631 nm and 642–690 nm for Alexa Fluor 633, respectively. dFBN somata were identified manually in the green channel, which was then thresholded, despeckled, and binarized by an automated custom macro in Fiji. The mitochondria-associated fraction of endogenous FLAG-tagged Drp1 in dFBNs was quantified in summed z-stacks as the proportion of red-fluorescent pixels within the somatic volume that colocalized with mitochondrial objects.

Electrophysiology. For whole-cell patch-clamp recordings *in vivo*, female flies aged 2–4 days post eclosion were prepared as for functional imaging, but the perineural sheath was also removed for electrode access. The GFP-labelled somata of dFBNs were visually targeted with borosilicate glass electrodes (8–10 MΩ) filled with internal solution (pH 7.3, 265 mOsM) containing (in mM): 10 HEPES, 140 potassium aspartate, 1 KCl, 4 MgATP, 0.5 Na_3GTP, 1 EGTA, and 10 biocytin. Signals were acquired at room temperature (23 °C) in current-clamp mode with a MultiClamp 700B amplifier (Molecular Devices), lowpass-

filtered at 5 kHz, and sampled at 10 kHz using an Axon Digidata 1550B digitizer controlled through pCLAMP 11.2 (Molecular Devices). Series resistances were monitored but not compensated. Data were analysed using the NeuroMatic package[108] (http://neuromatic.thinkrandom.com) in Igor Pro (WaveMetrics). Current–spike frequency functions were determined from voltage responses to a series of current steps (5-pA increments from –20 to 105 pA, 1 s duration) from a pre-pulse potential of –60 ± 5 mV. Spikes were detected by finding minima in the second derivative of the membrane potential trace. Spike frequencies were normalized to membrane resistances, which were calculated from linear fits of the steady-state voltage changes elicited by hyperpolarizing current steps. Only dFBNs firing more than one action potential in response to depolarizing current injections, with resting potentials below –30 mV and series resistances remaining below 50 MΩ throughout the recording, were characterized further. Spike bursts were defined as sets of spikes with an average intra-burst inter-spike interval (ISI) <50 ms and an inter-burst ISI >100 ms. These ISI thresholds were set after visual inspection of voltage traces of all recorded neurons. Cells were scored as bursting if they generated at least one action potential burst during the series of depolarizing current steps.

Analysis of mitochondria in volume electron micrographs. The hemibrain v1.2.1 connectome[30] was accessed in neuPrint+ (ref. [109]). The volumes of mitochondria in all *R23E10-GAL4*-labeled dFBNs[110] and uniglomerular olfactory PNs[30] in the left hemisphere (which contains mostly the dendritic compartments) were retrieved via Neo4j Cypher and neuPrint-python queries and analysed with custom MATLAB scripts.

Quantification and statistical analysis. Gene expression levels were compared by Bonferroni-corrected Wilcoxon rank-sum test. Gene ontology enrichment was quantified using Fisher's exact test in PANTHER (with a false discovery rate-adjusted significance level of $P < 0.05$) or ViSEAGO (with an unadjusted significance level of $P < 0.001$).

Behavioral, imaging, and electrophysiological data were analysed in Prism 10 (GraphPad) and SPSS Statistics 29 (IBM). All null hypothesis tests were two-sided. To control type I errors, *P*-values were adjusted to achieve a joint α of 0.05 at each level in a hypothesis hierarchy; multiplicity-adjusted *P*-values are reported in cases of multiple comparisons at one level. Group means were compared by *t* test, one-way ANOVA, two-way repeated-measures ANOVA, or mixed-effects models, as stated, followed by planned pairwise analyses with

Holm-Šidák's multiple comparisons test where indicated. Repeated-measures ANOVA and mixed-effect models used the Geisser-Greenhouse correction. Where the assumption of normality was violated (as indicated by D'Agostino-Pearson test), group means were compared by Mann-Whitney test or Kruskal-Wallis ANOVA, followed by planned pairwise analyses using Dunn's multiple comparisons test, as indicated. Frequency distributions were analysed by χ^2 test, and categories responsible for pairwise differences were detected[111] by locating cells with standardized residuals ≥ 2.

The investigators were blind to sleep history and/or genotype in imaging experiments but not otherwise. Sample sizes in behavioral experiments (typically n=32 flies per genotype) were chosen to detect 2-h differences in daily sleep with a power of 0.9. All behavioral experiments were run at least three times, on different days and with different batches of flies. The figures show pooled data from all replicates.

Acknowledgments

We thank C. Talbot for instrumentation; L. Ballenberger, K. Christodoulou, C. Hartmann, A. Krebbers, Y. Siu, and T. Wong for help with genetics and dissections; W. Budenberg for support in customizing the Zantiks MWP unit; the Don Mason Facility of Flow Cytometry and the Light Microscopy Facility, Sir William Dunn School of Pathology, University of Oxford, for cell sorting and access to the Olympus SoRa microscope, respectively; the Oxford Genomics Center at the Wellcome Center for Human Genetics (funded by Wellcome grant 203141/A/16/Z) for RNA sequencing; the Oxford Micron Bioimaging Facility (funded by Wellcome grants 091911/B/10/Z and 107457/Z/15/Z) for access to the Zeiss LSM980 microscope; H. Bellen, S. Bullock, J. Chung, T. Clandinin, R. Davis, M. Feany, M. Guo, Y. Imai, H. Jacobs, Y. Jan, V. Jayaraman, L. Luo, J. McNew, G. Rubin, W. Saxton, R. Stowers, S. Waddell, A. Whitworth, the Bloomington Stock Center, the Vienna *Drosophila* Resource Center, the Transgenic RNAi Project (TRiP), and the FlyORF Zurich ORFeome Project for flies; V. Croset, C. Treiber, and S. Waddell for advice on single-cell RNA sequencing; the FlyLight Project Team at Janelia Research Campus for anatomical images reproduced in Fig. S 1g; and T. Calì, P. Hasenhuetl, R. Klemm, V. Savage, and E. Vrontou for discussions. This work was supported by grants from the European Research Council (832467) and Wellcome (209235/Z/17/Z and 106988/Z/15/Z) to G. M.; R. S. held a Wellcome Four-Year PhD

Studentship in Basic Science (215200/Z/19/Z) and A.K. postdoctoral fellowships from the Swiss National Science Foundation and EMBO.

Author contributions

R.S. performed and analysed all transcriptomic, imaging, and behavioral experiments and C.D.V. all electrophysiological recordings; R.S. analysed volume electron microscopy data; N.M. assisted with imaging, genetics, and behavior; A. K. conducted initial studies with Ucp4. R.S. and G.M. designed the study, interpreted the results, and prepared the manuscript. G.M. devised and directed the research and wrote the paper.

Correspondence and requests for materials should be addressed to G.M. (gero.miesenboeck@cncb.ox.ac.uk).

References

1. Steriade, M., Timofeev, I. & Grenier, F. Natural waking and sleep states: A view from inside neocortical neurons. *J Neurophysiol* **85**, 1969-1985 (2001).
2. Vyazovskiy, V. V. et al. Cortical firing and sleep homeostasis. *Neuron* **63**, 865-878 (2009).
3. Tononi, G. & Cirelli, C. Sleep and the price of plasticity: From synaptic and cellular homeostasis to memory consolidation and integration. *Neuron* **81**, 12-34 (2014).
4. de Vivo, L. et al. Loss of sleep affects the ultrastructure of pyramidal neurons in the adolescent mouse frontal cortex. *Sleep* **39**, 861-874 (2016).
5. Aboufares El Alaoui, A. et al. Increased interaction between endoplasmic reticulum and mitochondria following sleep deprivation. *BMC Biol* **21**, 1 (2023).
6. Haynes, P. R. et al. A neuron-glia lipid metabolic cycle couples daily sleep to mitochondrial homeostasis. *Nat Neurosci* **27**, 666-678 (2024).
7. Reich, P., Geyer, S. J. & Karnovsky, M. L. Metabolism of brain during sleep and wakefulness. *J Neurochem* **19**, 487-497 (1972).
8. Porkka-Heiskanen, T. et al. Adenosine: A mediator of the sleep-inducing effects of prolonged wakefulness. *Science* **276**, 1265-1268 (1997).
9. Cirelli, C., Gutierrez, C. M. & Tononi, G. Extensive and divergent effects of sleep and wakefulness on brain gene expression. *Neuron* **41**, 35-43 (2004).
10. Dopp, J. et al. Single-cell transcriptomics reveals that glial cells integrate homeostatic and circadian processes to drive sleep-wake cycles. *Nat Neurosci* **27**, 359-372 (2024).
11. von Economo, C. Die Pathologie des Schlafes. (eds Adler, L. et al.) 591-610 (Springer, Berlin, Heidelberg, 1926).
12. Macosko, E. Z. et al. Highly parallel genome-wide expression profiling of individual cells using nanoliter droplets. *Cell* **161**, 1202-1214 (2015).
13. Donlea, J. M., Thimgan, M. S., Suzuki, Y., Gottschalk, L. & Shaw, P. J. Inducing sleep by remote control facilitates memory consolidation in *Drosophila*. *Science* **332**, 1571-1576 (2011).
14. Hasenhuetl, P. S. et al. A half-center oscillator encodes sleep pressure. *BioRxiv* 2024.02.23.581780 (2024).
15. Donlea, J. M., Pimentel, D. & Miesenböck, G. Neuronal machinery of sleep homeostasis in *Drosophila*. *Neuron* **81**, 860-872 (2014).
16. Chen, N. et al. Widespread posttranscriptional regulation of cotransmission. *Sci Adv* **9**, eadg9836 (2023).
17. Donlea, J. M. et al. Recurrent circuitry for balancing sleep need and sleep. *Neuron* **97**, 378-389.e4 (2018).
18. Pimentel, D. et al. Operation of a homeostatic sleep switch. *Nature* **536**, 333-337 (2016).
19. Qian, Y. et al. Sleep homeostasis regulated by 5HT2b receptor in a small subset of neurons in the dorsal fan-shaped body of drosophila. *eLife* **6**, e26519 (2017).
20. Harrell, E. R., Pimentel, D. & Miesenböck, G. Changes in presynaptic gene expression during homeostatic compensation at a central synapse. *J Neurosci* **41**, 3054-3067 (2021).
21. Kempf, A., Song, S. M., Talbot, C. B. & Miesenböck, G. A potassium channel β-subunit couples mitochondrial electron transport to sleep. *Nature* **568**, 230-234 (2019).
22. Rorsman, H. O. et al. Sleep pressure accumulates in a voltage-gated lipid peroxidation memory. *BioRxiv* 2024.02.25.581768 (2024).

23. Balaban, R. S., Nemoto, S. & Finkel, T. Mitochondria, oxidants, and aging. *Cell* **120**, 483-495 (2005).
24. Willems, P. H., Rossignol, R., Dieteren, C. E., Murphy, M. P. & Koopman, W. J. Redox homeostasis and mitochondrial dynamics. *Cell Metab* **22**, 207-218 (2015).
25. Chance, B., Sies, H. & Boveris, A. Hydroperoxide metabolism in mammalian organs. *Physiol Rev* **59**, 527-605 (1979).
26. Maxwell, D. P., Wang, Y. & McIntosh, L. The alternative oxidase lowers mitochondrial reactive oxygen production in plant cells. *Proc Natl Acad Sci U S A* **96**, 8271-8276 (1999).
27. Heaton, G. M., Wagenvoord, R. J., Kemp, A. & Nicholls, D. G. Brown-adipose-tissue mitochondria: Photoaffinity labelling of the regulatory site of energy dissipation. *Eur J Biochem* **82**, 515-521 (1978).
28. Hara, K. Y., Wada, T., Kino, K., Asahi, T. & Sawamura, N. Construction of photoenergetic mitochondria in cultured mammalian cells. *Sci Rep* **3**, 1635 (2013).
29. Azuma, T. & Kei, T. Super-resolution spinning-disk confocal microscopy using optical photon reassignment. *Opt Express* **23**, 15003-15011 (2015).
30. Scheffer, L. K. et al. A connectome and analysis of the adult *Drosophila* central brain. *Elife* **9**, e57443 (2020).
31. Bleazard, W. et al. The dynamin-related GTPase Dnm1 regulates mitochondrial fission in yeast. *Nat Cell Biol* **1**, 298-304 (1999).
32. Sesaki, H. & Jensen, R. E. Division versus fusion: Dnm1p and Fzo1p antagonistically regulate mitochondrial shape. *J Cell Biol* **147**, 699-706 (1999).
33. Smirnova, E., Griparic, L., Shurland, D. L. & van der Bliek, A. M. Dynamin-related protein Drp1 is required for mitochondrial division in mammalian cells. *Mol Biol Cell* **12**, 2245-2256 (2001).
34. Jendrach, M., Mai, S., Pohl, S., Vöth, M. & Bereiter-Hahn, J. Short- and long-term alterations of mitochondrial morphology, dynamics and mtDNA after transient oxidative stress. *Mitochondrion* **8**, 293-304 (2008).
35. Abrisch, R. G., Gumbin, S. C., Wisniewski, B. T., Lackner, L. L. & Voeltz, G. K. Fission and fusion machineries converge at ER contact sites to regulate mitochondrial morphology. *J Cell Biol* **219**, e201911122 (2020).
36. Twig, G. et al. Fission and selective fusion govern mitochondrial segregation and elimination by autophagy. *EMBO J* **27**, 433-446 (2008).
37. Friedman, J. R. et al. ER tubules mark sites of mitochondrial division. *Science* **334**, 358-362 (2011).
38. Vance, J. E. Phospholipid synthesis in a membrane fraction associated with mitochondria. *J Biol Chem* **265**, 7248-7256 (1990).
39. Kornmann, B. et al. An ER-mitochondria tethering complex revealed by a synthetic biology screen. *Science* **325**, 477-481 (2009).
40. Chen, H., Chomyn, A. & Chan, D. C. Disruption of fusion results in mitochondrial heterogeneity and dysfunction. *J Biol Chem* **280**, 26185-26192 (2005).
41. Ryu, K. W. et al. Cellular ATP demand creates metabolically distinct subpopulations of mitochondria. *Nature* **635**, 746-754 (2024).
42. Hales, K. G. & Fuller, M. T. Developmentally regulated mitochondrial fusion mediated by a conserved, novel, predicted GTPase. *Cell* **90**, 121-129 (1997).
43. Hwa, J. J., Hiller, M. A., Fuller, M. T. & Santel, A. Differential expression of the *Drosophila* mitofusin genes *fuzzy onions* (*fzo*) and *dmfn*. *Mech Dev* **116**, 213-216 (2002).
44. Cipolat, S., Martins de Brito, O., Dal Zilio, B. & Scorrano, L. OPA1 requires mitofusin 1 to promote mitochondrial fusion. *Proc Natl Acad Sci U S A* **101**, 15927-15932 (2004).

45. Choi, S. Y. et al. A common lipid links Mfn-mediated mitochondrial fusion and SNARE-regulated exocytosis. *Nat Cell Biol* **8**, 1255-1262 (2006).
46. Zhang, Y. et al. Mitoguardin regulates mitochondrial fusion through MitoPLD and is required for neuronal homeostasis. *Mol Cell* **61**, 111-124 (2016).
47. Kim, H., Lee, S., Jun, Y. & Lee, C. Structural basis for mitoguardin-2 mediated lipid transport at ER-mitochondrial membrane contact sites. *Nat Commun* **13**, 3702 (2022).
48. Hong, Z. et al. Mitoguardin-2-mediated lipid transfer preserves mitochondrial morphology and lipid droplet formation. *J Cell Biol* **221**, e202207022 (2022).
49. Sperling, E. A., Knoll, A. H. & Girguis, P. R. The ecological physiology of Earth's second oxygen revolution. *Annu. Rev. Ecol. Evol. Syst.* **46**, 215-235 (2015).
50. Galliot, B. & Quiquand, M. A two-step process in the emergence of neurogenesis. *Eur J Neurosci* **34**, 847-862 (2011).
51. Nath, R. D. et al. The jellyfish *Cassiopea* exhibits a sleep-like state. *Curr Biol* **27**, 2984-2990.e3 (2017).
52. Savage, V. M. & West, G. B. A quantitative, theoretical framework for understanding mammalian sleep. *Proc Natl Acad Sci U S A* **104**, 1051-1056 (2007).
53. Zepelin, H. & Rechtschaffen, A. Mammalian sleep, longevity, and energy metabolism. *Brain Behav Evol* **10**, 425-470 (1974).
54. West, G. B., Woodruff, W. H. & Brown, J. H. Allometric scaling of metabolic rate from molecules and mitochondria to cells and mammals. *Proc Natl Acad Sci U S A* **99 Suppl 1**, 2473-2478 (2002).
55. Dietrich, M. O., Liu, Z. W. & Horvath, T. L. Mitochondrial dynamics controlled by mitofusins regulate agrp neuronal activity and diet-induced obesity. *Cell* **155**, 188-199 (2013).
56. Jenett, A. et al. A GAL4-driver line resource for *Drosophila* neurobiology. *Cell Rep* **2**, 991-1001 (2012).
57. Luan, H., Peabody, N. C., Vinson, C. R. & White, B. H. Refined spatial manipulation of neuronal function by combinatorial restriction of transgene expression. *Neuron* **52**, 425-436 (2006).
58. Dionne, H., Hibbard, K. L., Cavallaro, A., Kao, J. C. & Rubin, G. M. Genetic reagents for making Split-GAL4 lines in *Drosophila*. *Genetics* **209**, 31-35 (2018).
59. Lacin, H. et al. Neurotransmitter identity is acquired in a lineage-restricted manner in the *Drosophila* CNS. *Elife* **8**, e43701 (2019).
60. Stocker, R. F., Heimbeck, G., Gendre, N. & de Belle, J. S. Neuroblast ablation in *Drosophila* P[GAL4] lines reveals origins of olfactory interneurons. *J Neurobiol* **32**, 443-456 (1997).
61. Tanaka, N. K., Tanimoto, H. & Ito, K. Neuronal assemblies of the *Drosophila* mushroom body. *J Comp Neurol* **508**, 711-755 (2008).
62. Berry, J. A., Cervantes-Sandoval, I., Chakraborty, M. & Davis, R. L. Sleep facilitates memory by blocking dopamine Neuron-Mediated forgetting. *Cell* **161**, 1656-1667 (2015).
63. Shearin, H. K., Macdonald, I. S., Spector, L. P. & Stowers, R. S. Hexameric GFP and mCherry reporters for the *Drosophila* GAL4, Q, and LexA transcription systems. *Genetics* **196**, 951-960 (2014).
64. Lee, T. & Luo, L. Mosaic analysis with a repressible cell marker for studies of gene function in neuronal morphogenesis. *Neuron* **22**, 451-461 (1999).
65. Rizzuto, R., Brini, M., Pizzo, P., Murgia, M. & Pozzan, T. Chimeric green fluorescent protein as a tool for visualizing subcellular organelles in living cells. *Curr Biol* **5**, 635-642 (1995).

66. Pilling, A. D., Horiuchi, D., Lively, C. M. & Saxton, W. M. Kinesin-1 and dynein are the primary motors for fast transport of mitochondria in *Drosophila* motor axons. *Mol Biol Cell* **17**, 2057-2068 (2006).
67. Vagnoni, A. & Bullock, S. L. A simple method for imaging axonal transport in aging neurons using the adult *Drosophila* wing. *Nat Protoc* **11**, 1711-1723 (2016).
68. Summerville, J. B. et al. The effects of ER morphology on synaptic structure and function in *Drosophila melanogaster*. *J Cell Sci* **129**, 1635-1648 (2016).
69. Han, C., Jan, L. Y. & Jan, Y. N. Enhancer-driven membrane markers for analysis of nonautonomous mechanisms reveal neuron-glia interactions in *Drosophila*. *Proc Natl Acad Sci U S A* **108**, 9673-9678 (2011).
70. Lobas, M. A. et al. A genetically encoded single-wavelength sensor for imaging cytosolic and cell surface ATP. *Nat Commun* **10**, 711 (2019).
71. Mann, K., Deny, S., Ganguli, S. & Clandinin, T. R. Coupling of activity, metabolism and behavior across the *Drosophila* brain. *Nature* **593**, 244-248 (2021).
72. Imamura, H. et al. Visualization of ATP levels inside single living cells with fluorescence resonance energy transfer-based genetically encoded indicators. *Proc Natl Acad Sci U S A* **106**, 15651-15656 (2009).
73. Tsuyama, T. et al. In vivo fluorescent adenosine 5'-triphosphate (ATP) imaging of *Drosophila melanogaster* and *Caenorhabditis elegans* by using a genetically encoded fluorescent ATP biosensor optimized for low temperatures. *Anal Chem* **85**, 7889-7896 (2013).
74. Fernandez-Ayala, D. J. M. et al. Expression of the *Ciona intestinalis* alternative oxidase (AOX) in *Drosophila* complements defects in mitochondrial oxidative phosphorylation. *Cell Metab* **9**, 449-460 (2009).
75. Imai, Y. et al. Light-driven activation of mitochondrial proton-motive force improves motor behaviors in a *Drosophila* model of Parkinson's disease. *Commun Biol* **2**, 424 (2019).
76. Zemelman, B. V., Lee, G. A., Ng, M. & Miesenböck, G. Selective photostimulation of genetically chARGed neurons. *Neuron* **33**, 15-22 (2002).
77. Klapoetke, N. C. et al. Independent optical excitation of distinct neural populations. *Nat Methods* **11**, 338-346 (2014).
78. Hamada, F. N. et al. An internal thermal sensor controlling temperature preference in *Drosophila*. *Nature* **454**, 217-220 (2008).
79. Burke, C. J. et al. Layered reward signalling through octopamine and dopamine in *Drosophila*. *Nature* **492**, 433-437 (2012).
80. Cieri, D. et al. SPLICS: A split green fluorescent protein-based contact site sensor for narrow and wide heterotypic organelle juxtaposition. *Cell Death Differ* **25**, 1131-1145 (2018).
81. Hewitt, V. L. et al. Decreasing pdzd8-mediated mito-ER contacts improves organismal fitness and mitigates $a\beta_{42}$ toxicity. *Life Sci Alliance* **5**, e202201531 (2022).
82. Allen, G. F., Toth, R., James, J. & Ganley, I. G. Loss of iron triggers PINK1/Parkin-independent mitophagy. *EMBO Rep* **14**, 1127-1135 (2013).
83. Lee, J. J. et al. Basal mitophagy is widespread in *Drosophila* but minimally affected by loss of Pink1 or Parkin. *J Cell Biol* **217**, 1613-1622 (2018).
84. Mao, W. et al. UCP4, a novel brain-specific mitochondrial protein that reduces membrane potential in mammalian cells. *FEBS Lett* **443**, 326-330 (1999).
85. Bischof, J. et al. A versatile platform for creating a comprehensive UAS-ORFeome library in *Drosophila*. *Development* **140**, 2434-2442 (2013).

86. Deng, H., Dodson, M. W., Huang, H. & Guo, M. The Parkinson's disease genes *pink1* and *parkin* promote mitochondrial fission and/or inhibit fusion in *Drosophila*. *Proc Natl Acad Sci U S A* **105**, 14503-14508 (2008).
87. Park, J., Lee, G. & Chung, J. The PINK1-Parkin pathway is involved in the regulation of mitochondrial remodeling process. *Biochem Biophys Res Commun* **378**, 518-523 (2009).
88. DuBoff, B., Götz, J. & Feany, M. B. Tau promotes neurodegeneration via DRP1 mislocalization in vivo. *Neuron* **75**, 618-632 (2012).
89. Sandoval, H. et al. Mitochondrial fusion but not fission regulates larval growth and synaptic development through steroid hormone production. *Elife* **3**, e03558 (2014).
90. Dietzl, G. et al. A genome-wide transgenic RNAi library for conditional gene inactivation in *Drosophila*. *Nature* **448**, 151-156 (2007).
91. Perkins, L. A. et al. The transgenic RNAi project at Harvard Medical School: Resources and validation. *Genetics* **201**, 843-852 (2015).
92. Verstreken, P. et al. Synaptic mitochondria are critical for mobilization of reserve pool vesicles at *Drosophila* neuromuscular junctions. *Neuron* **47**, 365-378 (2005).
93. Hendricks, J. C. et al. Rest in *Drosophila* is a sleep-like state. *Neuron* **25**, 129-138 (2000).
94. Shaw, P. J., Cirelli, C., Greenspan, R. J. & Tononi, G. Correlates of sleep and waking in *Drosophila melanogaster*. *Science* **287**, 1834-1837 (2000).
95. Vecsey, C. G., Koochagian, C., Porter, M. T., Roman, G. & Sitaraman, D. Analysis of sleep and circadian rhythms from *Drosophila* Activity-Monitoring data using SCAMP. *Cold Spring Harb Protoc* **2024**, pdb.prot108182 (2024).
96. Shaw, P. J., Tononi, G., Greenspan, R. J. & Robinson, D. F. Stress response genes protect against lethal effects of sleep deprivation in *Drosophila*. *Nature* **417**, 287-291 (2002).
97. Satija, R., Farrell, J. A., Gennert, D., Schier, A. F. & Regev, A. Spatial reconstruction of single-cell gene expression data. *Nat Biotechnol* **33**, 495-502 (2015).
98. Croset, V., Treiber, C. D. & Waddell, S. Cellular diversity in the *Drosophila* midbrain revealed by single-cell transcriptomics. *eLife* **7**, e34550 (2018).
99. Hao, Y. et al. Integrated analysis of multimodal single-cell data. *Cell* **184**, 3573-3587.e29 (2021).
100. Davie, K. et al. A Single-Cell transcriptome atlas of the aging *Drosophila* brain. *Cell* **174**, 982-998.e20 (2018).
101. Konstantinides, N. et al. Phenotypic convergence: Distinct transcription factors regulate common terminal features. *Cell* **174**, 622-635.e13 (2018).
102. Wang, J. Z., Du, Z., Payattakool, R., Yu, P. S. & Chen, C. F. A new method to measure the semantic similarity of GO terms. *Bioinformatics* **23**, 1274-1281 (2007).
103. Chaudhry, A., Shi, R. & Luciani, D. S. A pipeline for multidimensional confocal analysis of mitochondrial morphology, function, and dynamics in pancreatic β-cells. *Am J Physiol Endocrinol Metab* **318**, E87-E101 (2020).
104. Kirshner, H., Aguet, F., Sage, D. & Unser, M. 3-D PSF fitting for fluorescence microscopy: Implementation and localization application. *J Microsc* **249**, 13-25 (2013).
105. Dey, N. et al. Richardson-Lucy algorithm with total variation regularization for 3D confocal microscope deconvolution. *Microsc Res Tech* **69**, 260-266 (2006).
106. Sage, D. et al. DeconvolutionLab2: An open-source software for deconvolution microscopy. *Methods* **115**, 28-41 (2017).
107. Calì, T. & Brini, M. Quantification of organelle contact sites by split-GFP-based contact site sensors (SPLICS) in living cells. *Nat Protoc* **16**, 5287-5308 (2021).

108. Rothman, J. S. & Silver, R. A. NeuroMatic: An integrated open-source software toolkit for acquisition, analysis and simulation of electrophysiological data. *Front Neuroinform* **12**, 14 (2018).
109. Plaza, S. M. et al. NeuPrint: An open access tool for EM connectomics. *Front Neuroinform* **16**, 896292 (2022).
110. Hulse, B. K. et al. A connectome of the *Drosophila* central complex reveals network motifs suitable for flexible navigation and context-dependent action selection. *Elife* **10**, e66039 (2021).
111. Agresti, A. *Categorical Data Analysis.* (John Wiley & Sons, Hoboken, 2013).

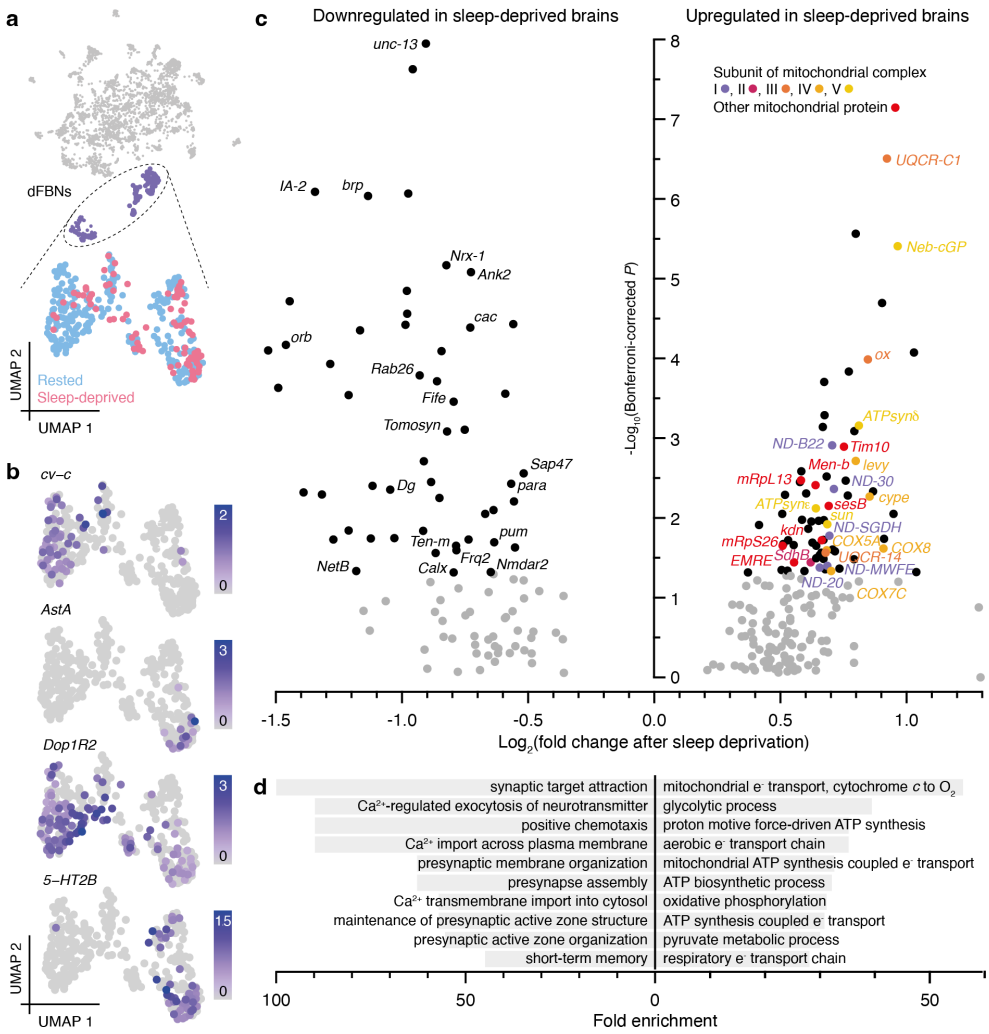

Fig. 1 | The transcriptional response of dFBNs to sleep deprivation.

a, Uniform manifold approximation and projection (UMAP) representation of glutamatergic neurons (gray) according to their gene expression profiles. dFBNs (top, purple) form a distinct cluster containing cells from rested (blue, *n*=237 cells) and sleep-deprived (red, *n*=86 cells) brains (bottom). **b**, Log-normalized expression levels of dFBN markers. **c**, Volcano plot of sleep history-dependent gene expression changes in dFBNs. Signals with Bonferroni-corrected *P*<0.05 are indicated in black; labels identify protein products localized to synapses or mitochondria; colors denote subunits of mitochondrial respiratory complexes. The *P*-value of *unc-13* exceeds the y-axis limit and is plotted at the top of the graph. **d**, Enrichment of the top 10 downregulated (left) and upregulated (right) 'biological process' gene ontology terms in the set of differentially expressed dFBN genes.

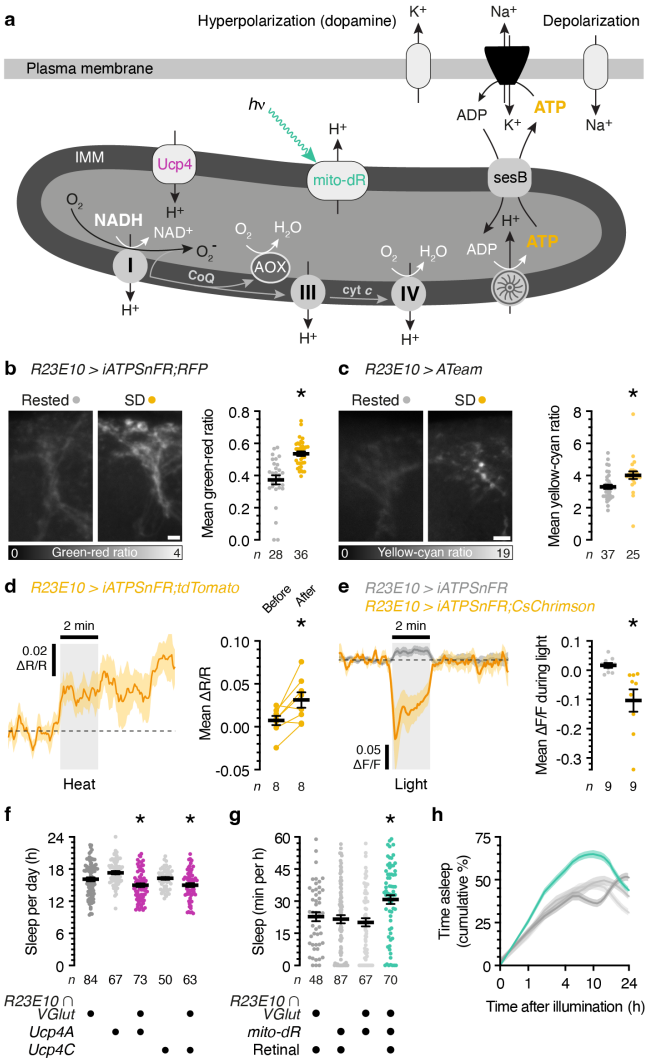

.

Fig. 2 | A mitochondrial electron surplus relative to ATP demand induces sleep.

a, Proton-pumping complexes I, III, and IV convert the energy of electron transfers from NADH to O_2 —via intermediates coenzyme Q (CoQ) and cytochrome *c* (cyt *c*)—into a proton electrochemical gradient Δp across the inner mitochondrial membrane (IMM). Uncoupling protein 4 (Ucp4) discharges, while illumination of mito-dR charges, the IMM. The return of extruded protons to the matrix spins the blades of the ATP synthase and produces ATP, which leaves the matrix via sesB in exchange for cytoplasmic ADP. Neuronal ATP consumption is activity-dependent and dominated by the plasma membrane Na^+/K^+ ATPase, which restores ion gradients diminished by action and excitatory synaptic currents. An oversupply (relative to ATP demand) of electrons to CoQ increases the risk of single-electron reductions of O_2 to O_2^- at complexes I and III. AOX mitigates this risk. **b**, **c**, Summed-intensity projections of dFBN dendrites expressing iATPSnFR plus RFP (**b**) or ATeam (**c**), in rested and sleep-deprived (SD) flies. Scale bars, 5 μm. Emission ratios are intensity-coded according to the keys below and increase after sleep deprivation (**b**, $P<0.0001$; **c**, $P=0.0003$; two-sided Mann-Whitney test). **d**, Arousing heat elevates ATP in dFBNs expressing iATPSnFR plus tdTomato. Mean fluorescence was quantified in 20-s windows immediately before and after stimulation ($P=0.0152$, two-sided paired *t*-test). **e**, Optogenetic stimulation dissipates ATP in dFBNs expressing iATPSnFR and CsChrimson, but not in

dFBNs lacking CsChrimson (P=0.0076, two-sided t-test). **f**, Sleep in flies expressing *R23E10* ∩ *VGlut-GAL4*-driven Ucp4A or Ucp4C and parental controls (P≤0.0381, Holm-Šídák test after ANOVA). **g**, **h**, Sleep during the first 60 min after illumination (**g**, P≤0.0432, Dunn's test after Kruskal-Wallis ANOVA) and cumulative sleep percentages in flies expressing *R23E10* ∩ *VGlut-GAL4*-driven mito-dR, with or without retinal, and parental controls (**h**, Δp photogeneration effect: P<0.0001, time × Δp photogeneration interaction: P<0.0001, two-way ANOVA). Asterisks indicate significant differences (P<0.05) from both parental controls or in planned pairwise comparisons. Data are means ± s.e.m.; n, number of dendritic regions (**b**, **c**) or flies (**d**–**h**). For statistical details see Supplementary Table 1.

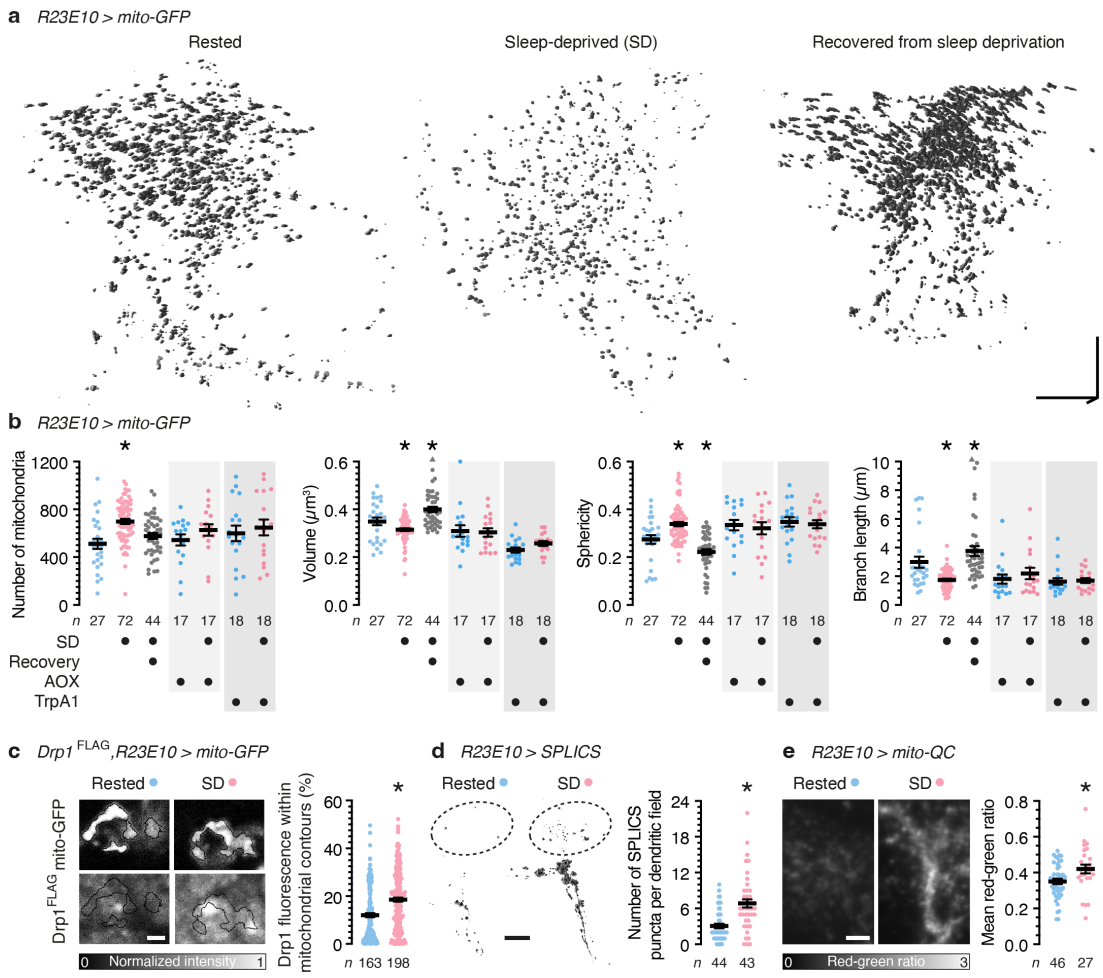

Fig. 3 | Sleep alters mitochondrial dynamics.

a, **b**, Volumetric renderings (**a**) and morphometric parameters (**b**) of automatically detected mitochondria in OPRM image stacks of dFBN dendrites in rested flies, sleep-deprived flies, and flies allowed to recover for 24 h after sleep deprivation. Scale bars, 10 μm. Sleep history-dependent changes in mitochondrial number (P<0.0001, Holm-Šídák test after ANOVA), volume (P=0.0470, Dunn's test after Kruskal-Wallis ANOVA), sphericity (P=0.0124, Dunn's test after Kruskal-Wallis ANOVA), and branch length (P=0.0033, Dunn's test after Kruskal-Wallis ANOVA) are occluded by the co-expression of AOX (P≥0.2257, two-sided t- or Mann-Whitney test) or the simultaneous activation of TrpA1 (P≥0.0625, two-sided t- or Mann-Whitney test) and (over)corrected after recovery sleep (number of mitochondria: P=0.1551, all other parameters: P≤0.0302, Dunn's test after Kruskal-Wallis ANOVA). Two data points exceeding the y-axis limits are plotted as triangles at the top of the graphs; mean and s.e.m. are based on the actual values. **c**, Drp1 recruitment. Single confocal image planes through dFBN somata of flies expressing *R23E10-GAL4*-driven mito-GFP (top) and Drp1^{FLAG} from the endogenous locus (bottom). Sleep deprivation increases the percentage of cellular anti-FLAG fluorescence (intensity-coded according to the key below) within automatically detected mitochondrial contours (P<0.0001, two-sided Mann-Whitney test). Scale bar, 2 μm. **d**, Mitochondria–ER contacts. Isosurface renderings (voxel value 128) of SPLICS puncta in distal dFBN dendritic branches (dashed outlines), obtained by trilinear interpolation of thresholded and despeckled confocal image stacks.

Sleep deprivation increases the number of SPLICS puncta per dendritic field ($P<0.0001$, two-sided Mann-Whitney test). Scale bar, 10 μm. **e**, Mitophagy. Summed-intensity projections of dFBN dendrites expressing mito-QC. Emission ratios are intensity-coded according to the key below and increase after sleep deprivation ($P=0.0101$, two-sided *t*-test). Scale bar, 5 μm. Data are means ± s.e.m.; *n*, number of dendritic regions (**b**, **d**, **e**) or somata (**c**); asterisks, significant differences ($P<0.05$) in planned pairwise comparisons. For statistical details see Supplementary Table 1.

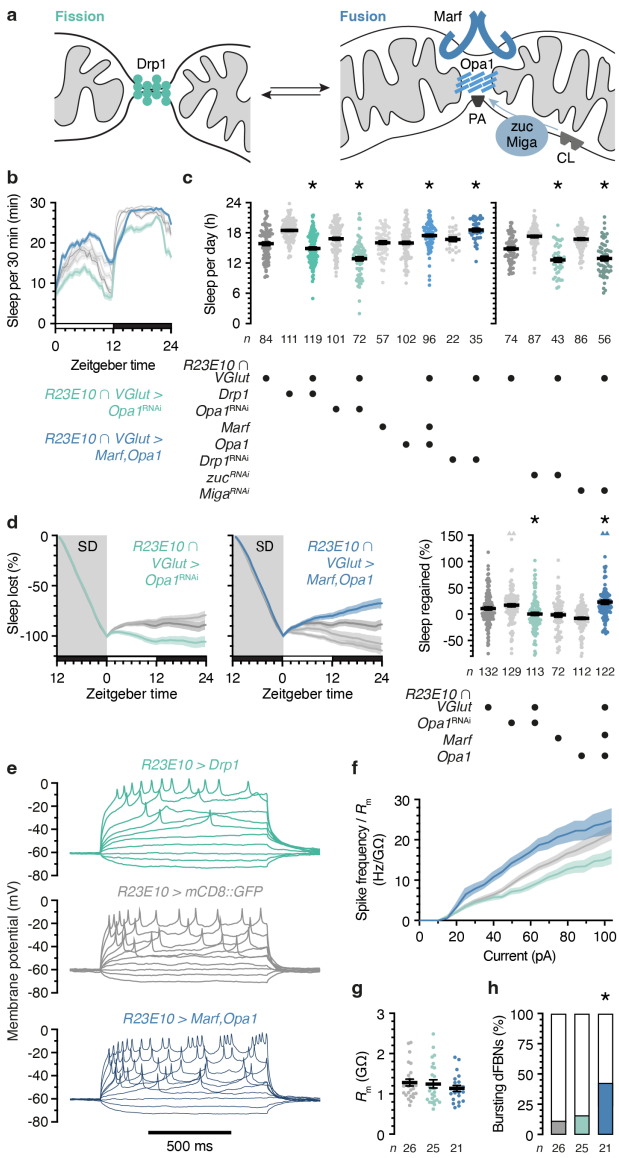

Fig. 4 | Mitochondrial dynamics alter sleep.

a, The mitochondrial fission (green) and fusion machineries (blue) comprise Drp1, the outer and inner membrane proteins Marf and Opa1, and the mitoPLD zuc, which releases phosphatidic acid (PA) from cardiolipin (CL). Miga stimulates zuc activity and/or directly supplies PA from other membranes. **b**, **c**, Sleep profiles (**b**, genotype effect: $P<0.0001$, time × genotype interaction: $P<0.0001$, two-way repeated-measures ANOVA) and daily sleep (**c**) in flies expressing *R23E10* ∩ *VGlut-GAL4*-driven fission or fusion proteins, or RNAi transgenes targeting transcripts encoding these proteins (left) or those regulating PA levels (right), and their parental controls. Manipulations that increase fission (green) or fusion (blue) alter sleep in opposite directions (GTPases: $P\leq0.0332$, Holm-Šídák test after ANOVA; PA regulators: $P\leq0.0198$ for all planned pairwise comparisons after Kruskal-Wallis ANOVA). **d**, Manipulations that increase fission (*R23E10* ∩ *VGlut-GAL4* > *Opa1*^{RNAi}, green) or fusion (*R23E10* ∩ *VGlut-GAL4* > *Marf;Opa1*, blue) alter the time courses (left panels, genotype effects: $P\leq0.0003$, time x genotype interactions: $P<0.0001$, two-way repeated-measures ANOVA) and percentages of sleep rebound after deprivation (SD) in opposite directions (right panel, genotype effect: $P\leq0.0450$ for

all planned pairwise comparisons after Kruskal-Wallis ANOVA). Four data points exceeding the y-axis limits are plotted as triangles at the top of the right-hand graph; mean and s.e.m. are based on the actual values. **e**, Example voltage responses to current steps of dFBNs expressing mCD8::GFP (gray) and Drp1 (green) or Marf plus Opa1 (blue). **f**, Manipulations that increase fission (green) or fusion (blue) alter the membrane resistance (R_m)-normalized spike frequency in opposite directions (genotype effect: $P<0.0001$, time × genotype interaction: $P<0.0001$, mixed-effects model, sample sizes in **g**). **g**, Membrane resistances (genotype effect: $P=0.5099$, ANOVA). **h**, The overexpression of Marf plus Opa1 increases the percentage of dFBNs generating bursts of action potentials ($P=0.0241$, χ^2 test; standardized residuals +2.01). Data are means ± s.e.m.; *n*, number of flies (**b**–**d**) or cells (**f**, **g**); asterisks, significant differences ($P<0.05$) in planned pairwise comparisons. For statistical details see Supplementary Table 1.

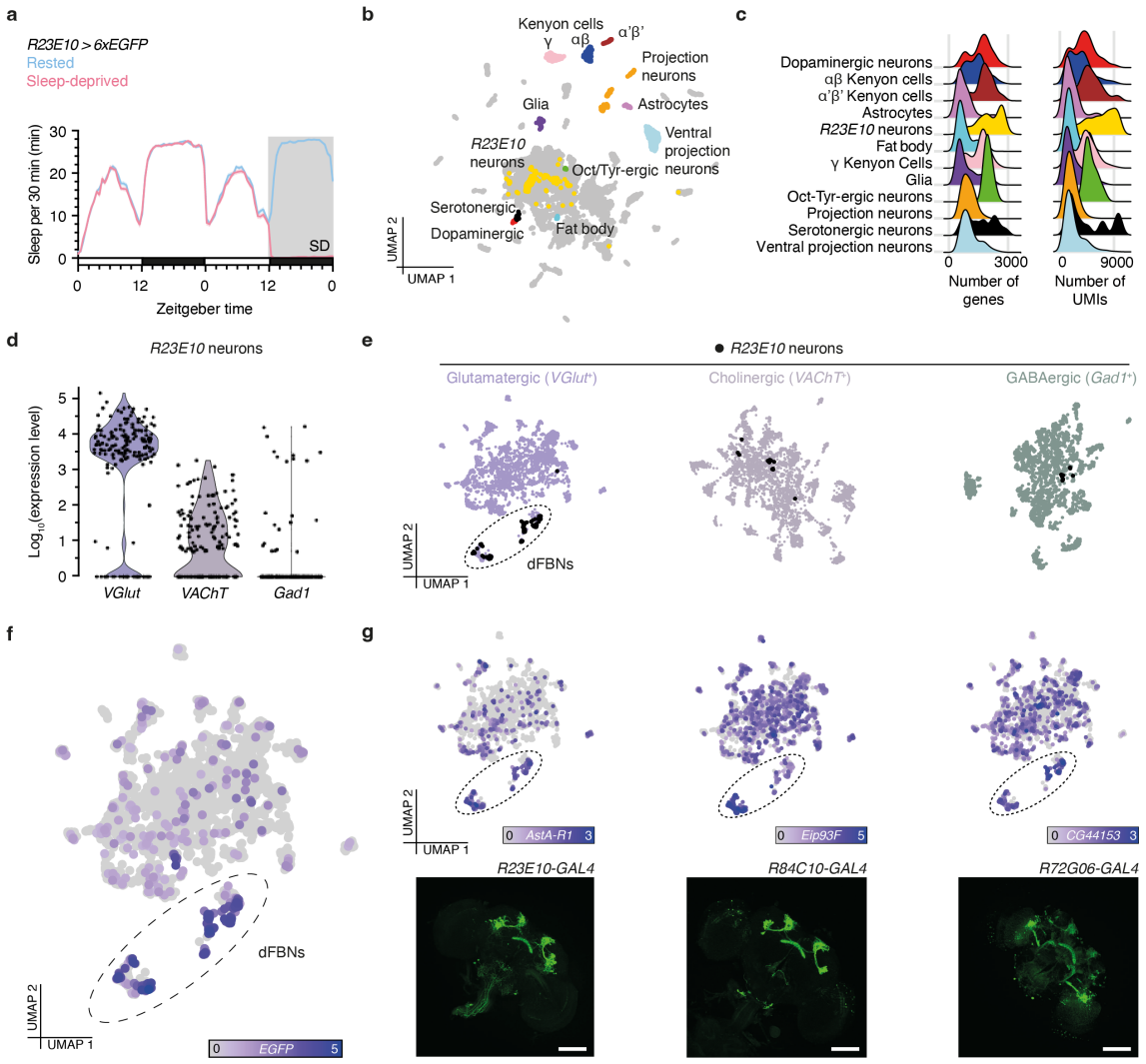

Fig. S 1 | Identification of dFBNs and their transcriptomic response to sleep deprivation by single-cell RNA-sequencing.

a, Sleep profiles of flies expressing *R23E10-GAL4*-driven 6xEGFP under control (blue, *n*=558) and sleep deprivation (SD) conditions (red, *n*=432) before single-cell RNA sequencing. **b**, Uniform manifold approximation and projection (UMAP) representation of cells in the fly brain. Highlighted cell types, including neurons nominated by *R23E10-GAL4* (yellow), were identified as detailed in Methods. **c**, Distribution of the number of unique molecular identifiers (UMIs) and genes per cell for each annotated cell type. **d**, Log-normalized distribution of the expression levels of markers for the fast-acting neurotransmitters glutamate, acetylcholine, and GABA in *R23E10-GAL4* neurons. **e**, *R23E10-GAL4* neurons (black) mapped onto re-clustered representations of cells expressing glutamatergic, cholinergic, and GABAergic markers. *Bona fide* dFBNs form a distinct glutamatergic cluster (dashed outline). **f**, **g**, Compared to the rest of the glutamatergic brain, dFBNs are enriched in EGFP (**f**) and transcripts of genes whose enhancer fragments label dFBNs in *GAL4* lines generated and imaged by the FlyLight project[56] (**g**). Log-normalized expression levels are color-coded according to the keys below each panel. Scale bars in **g**, 100 μm.

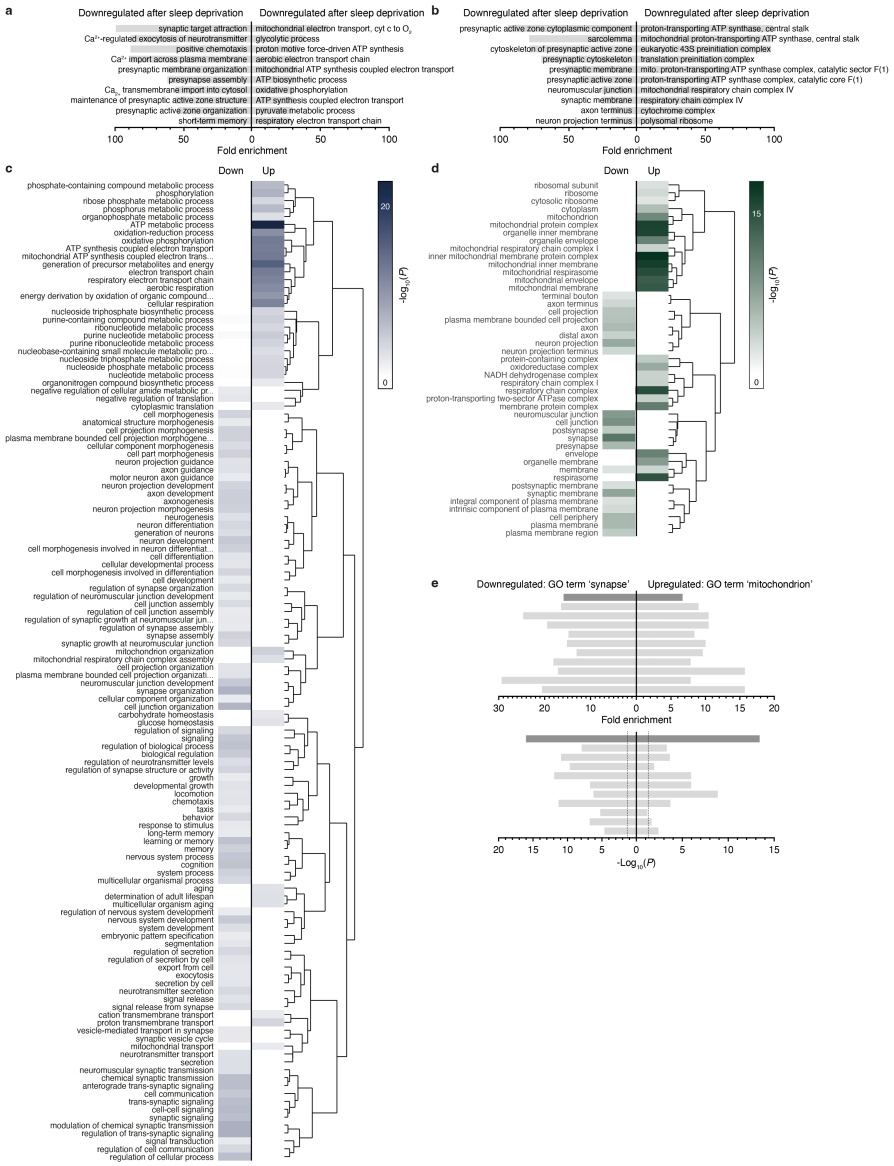

Fig. S 2 | Gene ontology analysis of sleep history-dependent gene expression in dFBNs. **a**–**d,** Enrichment of gene ontology (GO) 'biological process' (**a**, **c**) and 'cellular component' (**b**, **d**) terms in the set of genes whose expression in dFBNs varies with sleep history. Panels **a** and **b** plot the top 10 enriched terms by PANTHER Overrepresentation Test (fold enrichments >100 are truncated). Panels **c** and **d** show heatmaps (computed with ViSEAGO and topGO) of GO terms attached to downregulated (left) and upregulated (right) differentially expressed genes. Dendrograms represent semantic groupings among GO terms. *P*-values are color-coded according to the keys on the right. **e**, Enrichment (top) and uncorrected *P*-values (bottom, dotted lines at *P*=0.05) of the 'cellular component' GO terms 'mitochondrion' and 'synapse' in the sets of up- and downregulated genes by PANTHER Overrepresentation Test, in the full data set (dark gray) and after randomly downsampling (light gray) the number of rested dFBN transcriptomes to the number of sleep-deprived dFBN transcriptomes (*n*=86 cells in either condition). The downsampling process was repeated 10 times using the 'max.cells.per.ident' argument of the 'FindMarkers' function in Seurat, with reproducible seedings from 1 to 10.

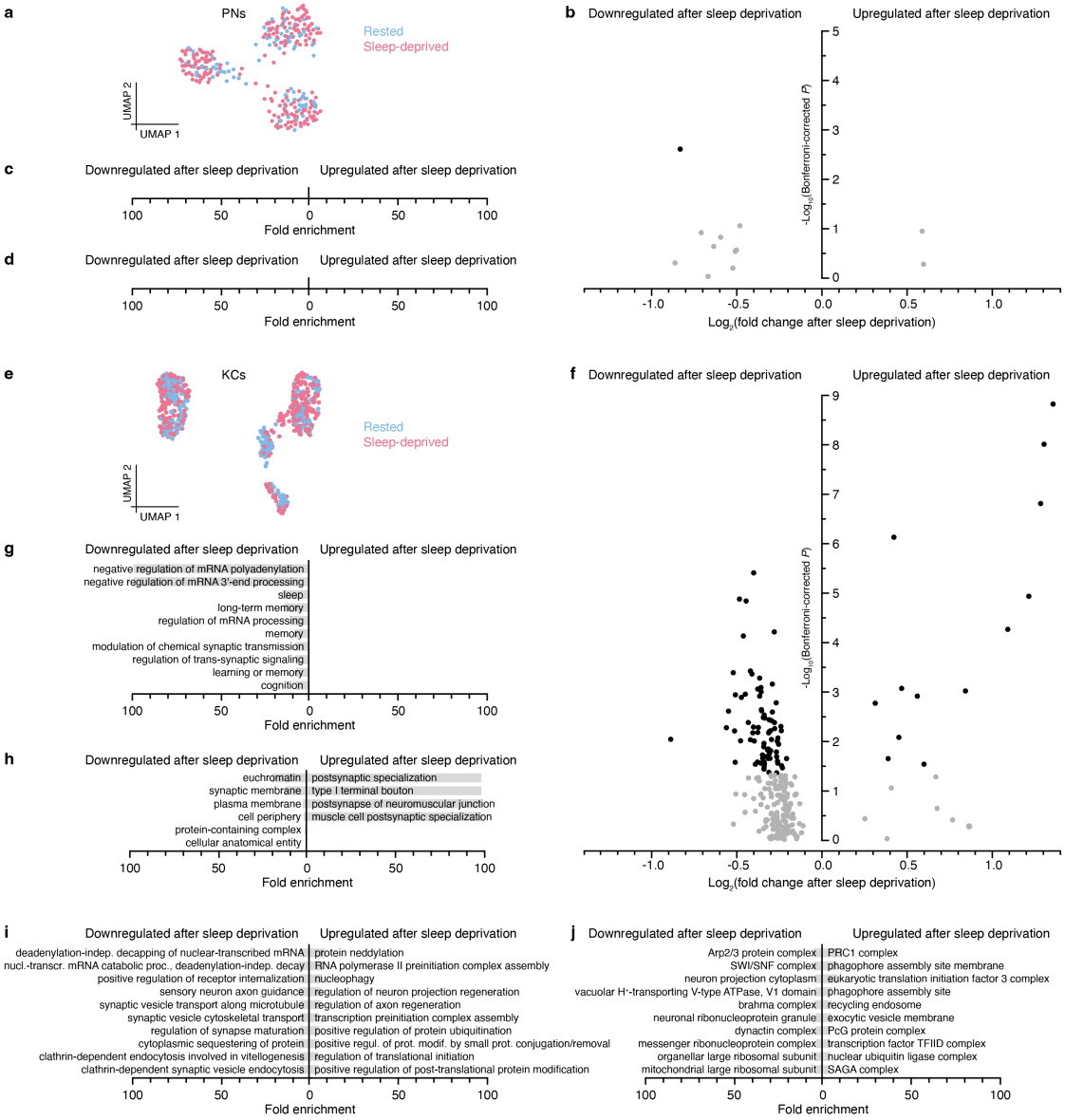

Fig. S 3 | Sleep history-dependent gene expression in KCs, PNs, and non-dFBN cells. **a**, UMAP representation of PNs (*n*=317) from rested (blue) and sleep-deprived brains (red) according to their gene expression profiles. **b**, Volcano plot of sleep history-dependent gene expression changes in PNs. A single signal with Bonferroni-corrected *P*<0.05 is indicated in black. **c**, **d**, PANTHER Overrepresentation Test fails to detect enriched 'biological process' (**g**) and 'cellular component' (**h**) gene ontology (GO) terms in the set of differentially expressed PN genes. **e**, UMAP representation of KCs (*n*=603) from rested (blue) and sleep-deprived brains (red) according to their gene expression profiles. **f**, Volcano plot of sleep history-dependent gene expression changes in PNs. Signal with Bonferroni-corrected *P*<0.05 are indicated in black. **g**, **h**, Enrichment of the top 10 downregulated and upregulated 'biological process' (**g**) and 'cellular component' (**h**) GO terms in the set of differentially expressed KC genes by PANTHER Overrepresentation Test (fold enrichments >100 are truncated). **i**, **j**, Enrichment of the top 10 downregulated and upregulated 'biological process' (**i**) and 'cellular component' (**j**) GO terms in the set of genes with differential expression in all non-dFBN cells by PANTHER Overrepresentation Test.

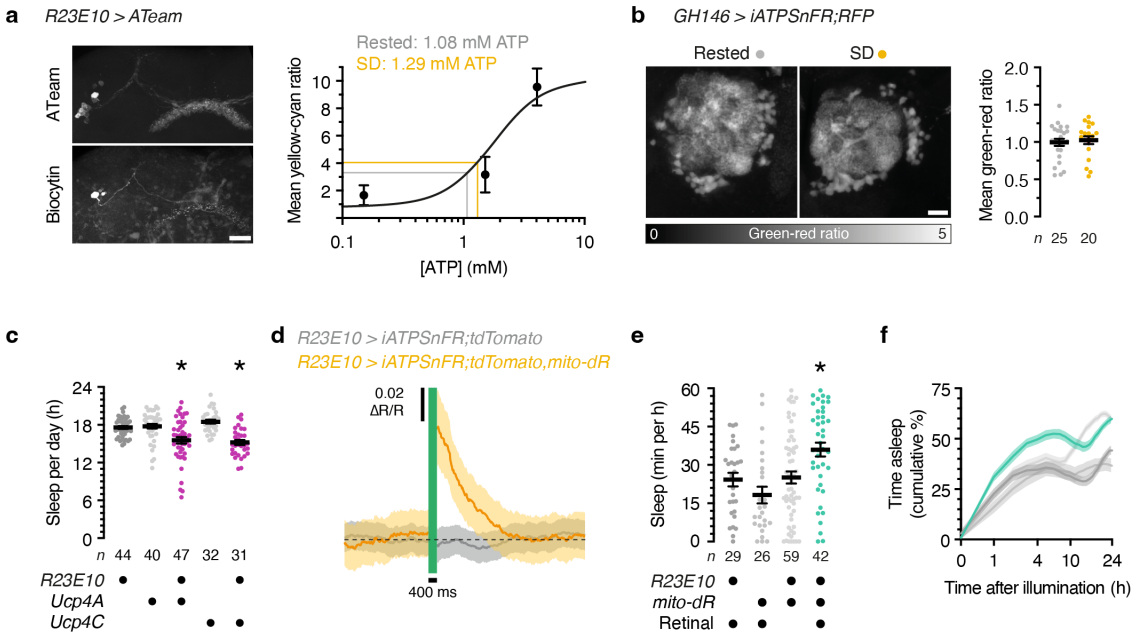

Fig. S 4 | Relationships between ATP levels, mitochondrial protonmotive force, and sleep in PNs and dFBNs.

a, Maximum-intensity projection of dFBNs expressing *R23E10-GAL4*-driven ATeam (top left, CFP channel). One dFBN has been filled with biocytin and a defined ATP concentration through a whole-cell electrode (bottom left). The right panel shows the least-squares fit of a Hill equation (dissociation constant 1.75 mM ATP, Hill coefficient 2.1) to the mean yellow-to-cyan emission ratio of biocytin-labelled dFBNs containing 0.15, 1.5, and 4 mM ATP (*n*=3 cells each). Scale bar, 20 μm. **b**, Summed-intensity projections of PN dendrites expressing iATPSnFR plus RFP, in rested and sleep-deprived (SD) flies. Emission ratios are intensity-coded according to the key below and unaltered by sleep deprivation (*P*=0.6616, two-sided *t*-test). Scale bar, 20 μm. **c**, Sleep in flies expressing *R23E10-GAL4*-driven Ucp4A or Ucp4C and parental controls (*P*≤0.0139, Dunn's test after Kruskal-Wallis ANOVA). **d**, A 400-ms pulse of green light elevates ATP in dFBNs expressing iATPSnFR plus tdTomato and mito-dR but not in dFBNs lacking mito-dR (*n*=5 flies of either genotype, Δ*p* photogeneration effect: *P*<0.0001, time × Δ*p* photogeneration interaction: *P*<0.0001, two-way ANOVA). **e**, **f**, Sleep during the first 60 min after illumination (**d**, *P*≤0.0279, Dunn's test after Kruskal-Wallis ANOVA) and cumulative sleep percentages in flies expressing *R23E10-GAL4*-driven mito-dR, with or without retinal, and parental controls (**e**, Δ*p* photogeneration effect: *P*<0.0001, time × Δ*p* photogeneration interaction: *P*<0.0001, mixed-effects model). Asterisks, significant differences (*P*<0.05) from both parental controls or in planned pairwise comparisons. Data are means ± s.e.m.; *n*, number of cells (**a**), antennal lobe glomeruli (**b**), or flies (**c**–**f**). For statistical details see Supplementary Table 2.

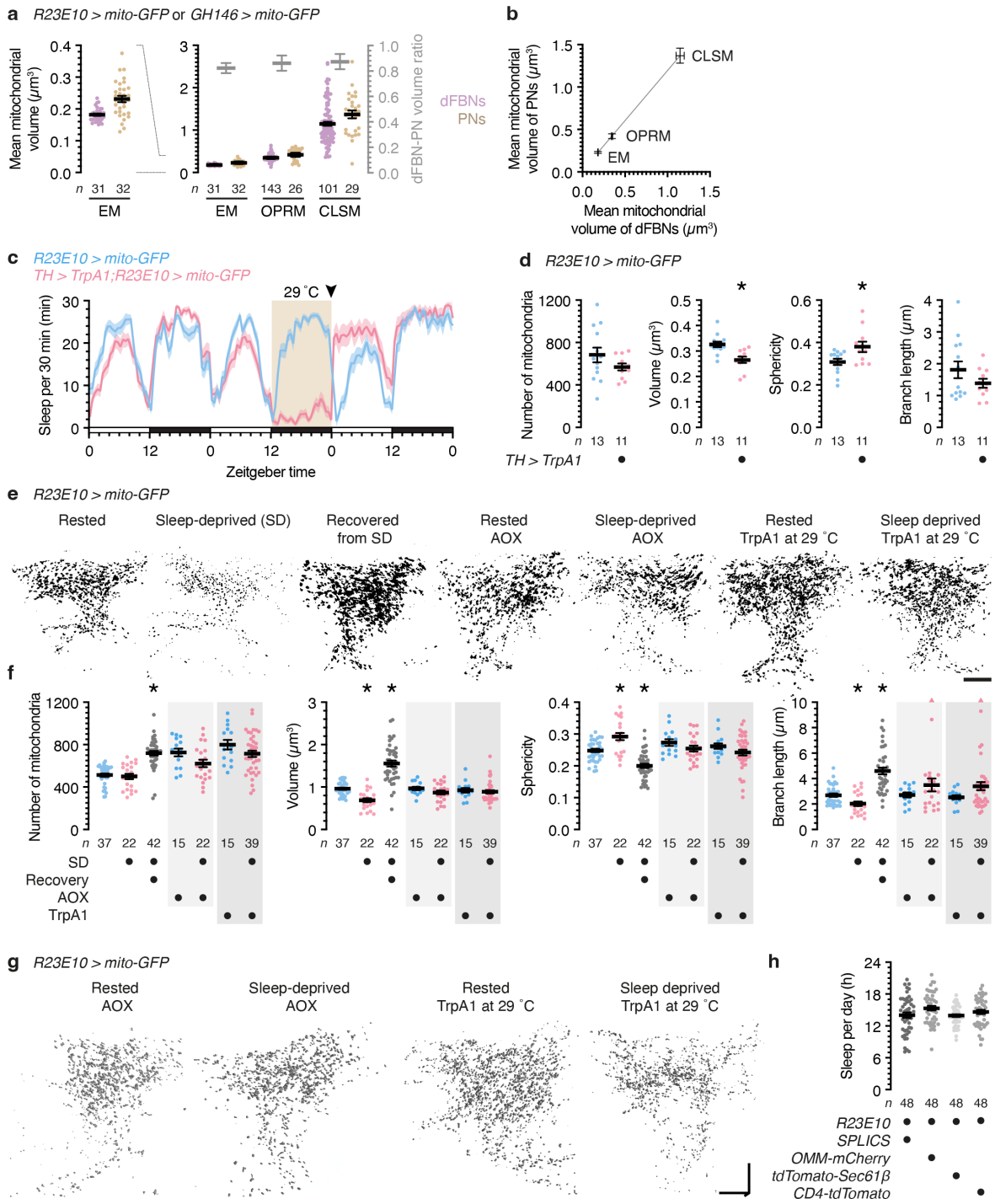

Fig. S 5 | Sleep alters the morphology of dFBN mitochondria.

a, Mean volumes (left y-axes) and volume ratios (right y-axis) of dFBN and PN mitochondria determined by volume electron microscopy (EM), optical photon reassignment microscopy (OPRM), and confocal laser-scanning microscopy (CLSM). **b**, Correlation between dFBN and PN mitochondrial volume estimates obtained by EM, OPRM, and CLSM (residual s.d. = 0.0041). EM data are from the hemibrain connectome[30]; OPRM and CLSM measurements of mitochondrial volumes in flies expressing mito-GFP are re-plotted from Fig. 3b and Fig. S 6b, and from **f** and Fig. S 6d, respectively. **c**, **d**, Sleep deprivation via thermogenetic activation of arousing dopaminergic neurons (**c**) causes

mitochondrial fragmentation detected by OPRM (**d**, number of mitochondria: P=0.1812, volume: P=0.0010, sphericity: P=0.0192, branch length: P=0.2013, two-sided t-test). Experimental and control flies (n=30 and 33, respectively) were reared and maintained at 21 ˚C and shifted to 29 ˚C between zeitgeber times 12 and 24 on day 2. The arrowhead marks the time point when 11 experimental and 13 control flies were removed and dissected for mitochondrial morphometry. **e**, **f**, Maximum intensity projections (**e**) and morphometric parameters (**f**) of automatically detected mitochondria in CLSM image stacks of dFBN dendrites in rested flies, sleep-deprived flies, flies allowed to recover for 24 h after sleep deprivation, and rested and sleep-deprived flies co-expressing *R23E10-GAL4*-driven AOX or TrpA1, which was activated at 29 ˚C. Scale bar, 10 μm. Sleep history-dependent changes in mitochondrial volume (P=0.0025, Holm-Šídák test after ANOVA), sphericity (P=0.0001, Holm-Šídák test after ANOVA), and branch length (P=0.0414, Holm-Šídák test after ANOVA) are occluded by the co-expression of AOX (P≥0.1515, two-sided t- or Mann-Whitney test) or the simultaneous activation of TrpA1 (P≥0.2002, two-sided t- or Mann-Whitney test) and overcorrected after recovery sleep (all parameters: P<0.0001, Holm-Šídák test after ANOVA). The number of mitochondria is unchanged by sleep deprivation (P>0.9999) but elevated after recovery sleep (P<0.0001, Dunn's test after Kruskal-Wallis ANOVA). Two data points exceeding the y-axis limits are plotted as triangles at the top of the graphs; mean and s.e.m. are based on the actual values. **g**, Volumetric renderings of automatically detected mitochondria in OPRM image stacks of dFBN dendrites in rested and sleep-deprived flies co-expressing *R23E10-GAL4*-driven AOX or TrpA1, which was activated at 29 ˚C. Scale bars, 10 μm. **h**, Sleep in flies expressing *R23E10-GAL4*-driven split-GFP-based contact site sensors (SPLICS) or fluorescent fusion proteins located in the outer mitochondrial (OMM), endoplasmic reticulum (Sec61β), or plasma membrane (CD4) (P=0.0648, ANOVA). Data are means ± s.e.m. or ratios of means ± error-propagated s.e.m. (**a**, light gray); n, number of cells (**a**, EM), dendritic fields (**a,** OPRM and CLSM, **d**, **f**), or flies (**c**, **h**); asterisks, significant differences (P<0.05) in planned pairwise comparisons. For statistical details see Supplementary Table 2.

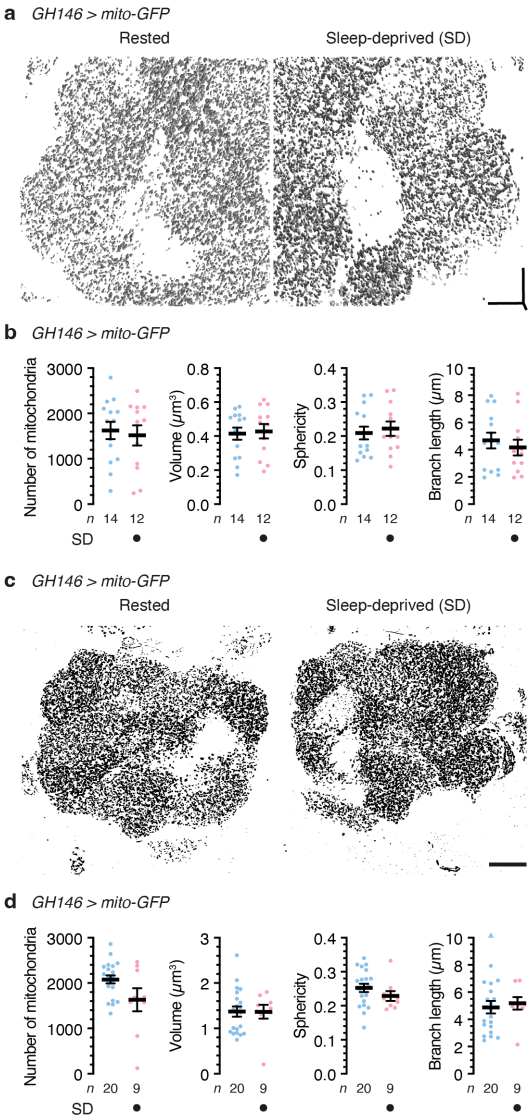

Fig. S 6 | Sleep does not alter the morphology of PN mitochondria.

a, **b**, Volumetric renderings (**a**) and morphometric parameters (**b**) of automatically detected mitochondria in OPRM image stacks of PN dendrites in rested and sleep-deprived flies. Scale bars, 10 μm. Mitochondrial number (P=0.7077, two-sided t-test), volume (P=0.8074, two-sided t-test), sphericity (P=0.6500, two-sided t-test), and branch length (P=0.5326, two-sided t-test) are unaffected by sleep deprivation. **c**, **d**, Maximum intensity projections (**c**) and morphometric parameters (**d**) of automatically detected mitochondria in CLSM image stacks of PN dendrites in rested and sleep-deprived flies. Scale bar, 20 μm. Mitochondrial number (P=0.2534, two-sided Mann-Whitney test), volume (P= 0.7637, two-sided Mann-Whitney test), sphericity (P=0.1953, two-sided Mann-Whitney test), and branch length (P=0.6972, two-sided t-test) are unaffected by sleep deprivation. One data point exceeding the y-axis limits is plotted as a triangle at the top of the right-hand graph; mean and s.e.m. are based on the actual values. For statistical details see Supplementary Table 2.

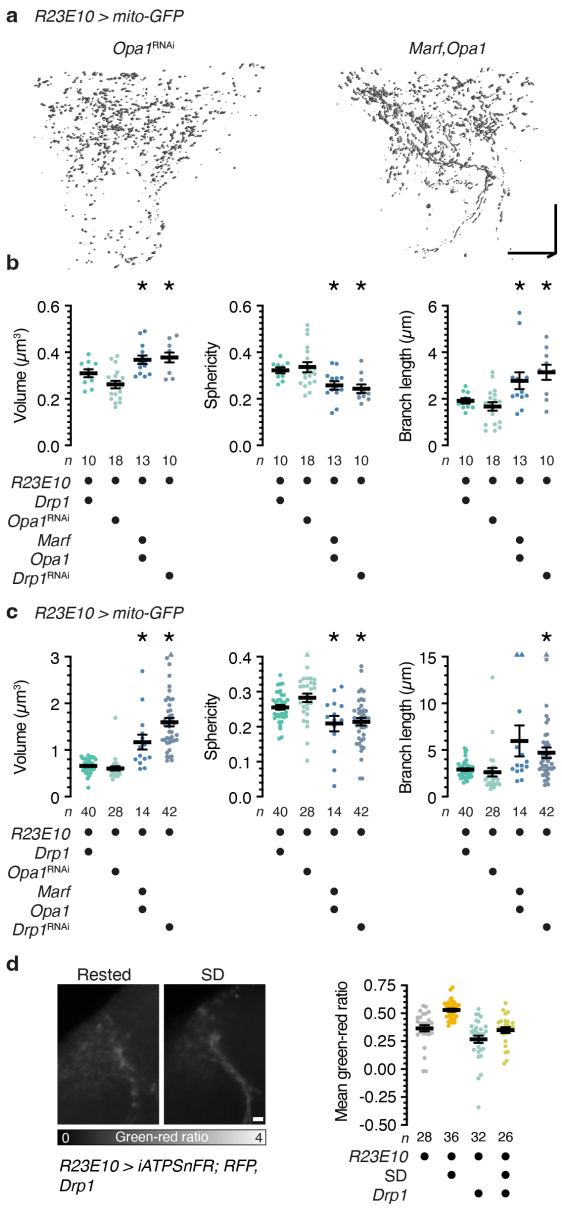

Fig. S 7 | Morphological and metabolic consequences of inducing mitochondrial fission or fusion in dFBNs.

a, **b**, Volumetric renderings (**a**) and morphometric parameters (**b**) of automatically detected mitochondria in OPRM image stacks of dFBN dendrites. Flies carried *R23E10-GAL4*-driven overexpression constructs or RNAi transgenes targeting mitochondrial fission or fusion machinery. Scale bars, 10 μm. Manipulations that increase fission (green) or fusion (blue) have opposite effects on mitochondrial volume ($P \leq 0.0480$, Holm-Šídák test after ANOVA), sphericity ($P \leq 0.0344$, Holm-Šídák test after ANOVA), and branch length ($P \leq 0.0326$, Holm-Šídák test after ANOVA). **c**, Morphometric parameters of automatically detected mitochondria in CLSM image stacks of dFBN dendrites. Flies carried *R23E10-GAL4*-driven overexpression constructs or RNAi transgenes targeting mitochondrial fission or fusion machinery. Manipulations that increase fission (green) or fusion (blue) have opposite effects on mitochondrial volume ($P \leq 0.0062$, Dunn's test after Kruskal-Wallis ANOVA), sphericity ($P \leq 0.0170$, Holm-Šídák test after ANOVA), and branch length ($P \leq 0.0427$, Dunn's test after

Kruskal-Wallis ANOVA). Five data points exceeding the y-axis limits are plotted as triangles at the top of the graphs; mean and s.e.m. are based on the actual values. **d**, Summed-intensity projections of dFBN dendrites expressing Drp1 and iATPSnFR plus RFP, in rested and sleep-deprived (SD) flies. Emission ratios are intensity-coded according to the key below and reduced in dFBNs expressing Drp1, irrespective of sleep history (Drp1 effect: $P<0.0001$, sleep history effect: $P<0.0001$, Drp1 × sleep history interaction: $P=0.1112$; two-way ANOVA). Scale bar, 5 μm. Data are means ± s.e.m.; *n*, number of dendritic fields; asterisks, significant differences ($P<0.05$) from both manipulations increasing fission. For statistical details see Supplementary Table 2.

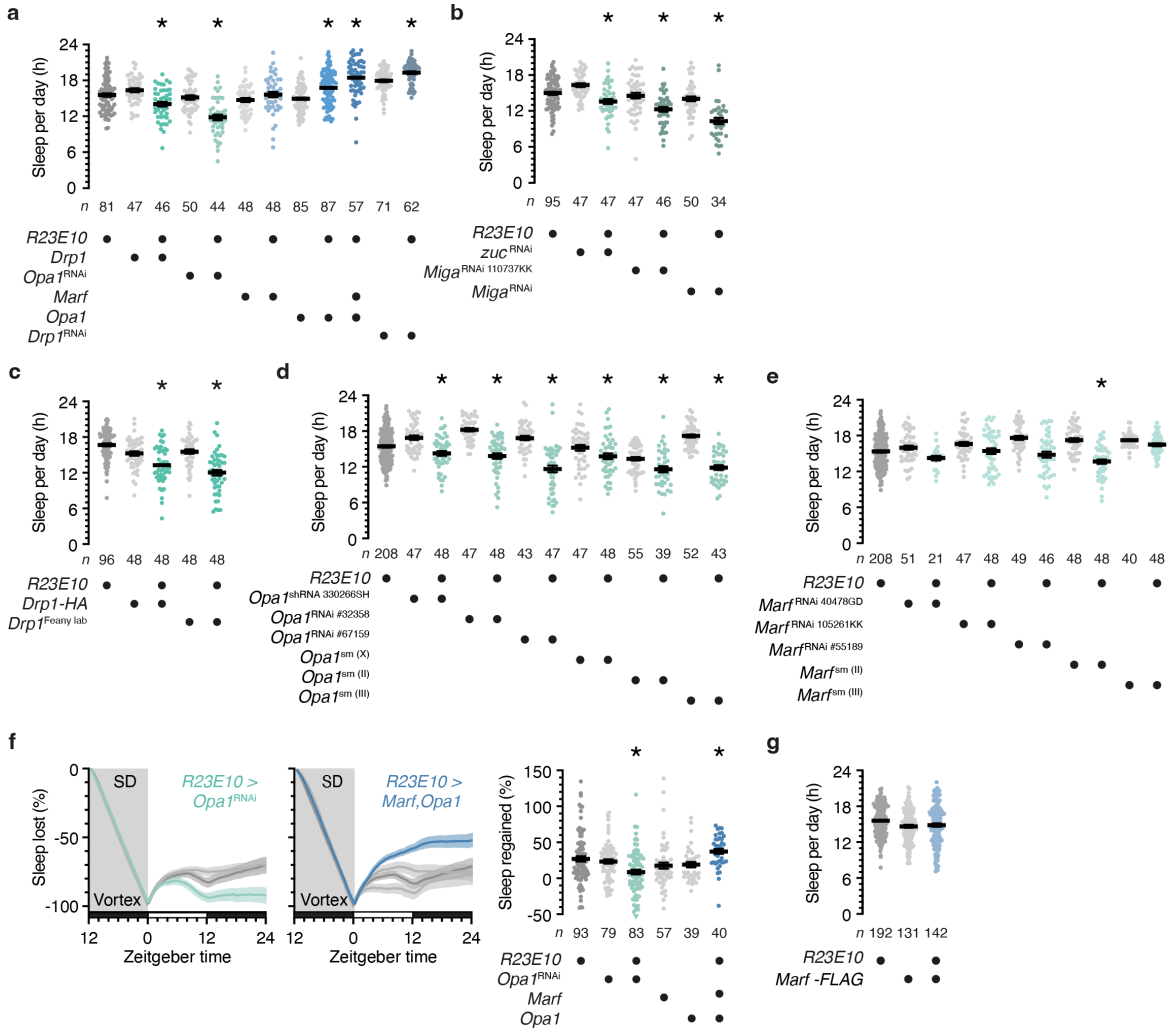

Fig. S 8 | Inducing mitochondrial fission or fusion in dFBNs alters sleep.

a, **b**, Sleep in flies expressing *R23E10-GAL4*-driven fission or fusion proteins, or RNAi transgenes targeting transcripts encoding these proteins (**a**) or proteins regulating PA levels (**b**), and their parental controls. With the exception of the overexpression of Marf alone ($P \geq 0.1622$, Holm-Šídák test after ANOVA), manipulations that increase fission (green) or fusion (blue) alter sleep in opposite directions (GTPases: $P \leq 0.0115$, PA regulators: $P \leq 0.0381$; Holm-Šídák test after ANOVA). **c**–**e**, Sleep in flies carrying *R23E10-GAL4*-driven Drp1 overexpression constructs or RNAi transgenes targeting mitochondrial fusion proteins not included in **a**, **b** and Fig. 4b: two independent constructs for Drp1 overexpression (**c**, $P \leq 0.0209$, Dunn's test after ANOVA); six independent RNAi transgenes directed against Opa1 (**d**, $P \leq 0.0199$, Holm-Šídák test after ANOVA); and five independent RNAi transgenes directed against Marf (**e**, $P \geq 0.1017$ relative to ≥1 parental control with the exception of *R23E10 > Marf* $^{sm(II)}$, Holm-Šídák test after ANOVA). **f**, Manipulations that increase fission (*R23E10-GAL4 > Opa1*^{RNAi}, green) or fusion (*R23E10 > Marf;Opa1*, blue) alter the time courses (left panels, genotype effects: $P \leq 0.0153$, time x genotype interactions: $P<0.0001$, two-way repeated-measures ANOVA) and percentages of sleep rebound after deprivation (SD) in opposite directions (right panel, genotype effect: $P \leq 0.0186$, Dunn's test after ANOVA). One data point exceeding the y-axis limits is plotted as a

triangle at the bottom of the right-hand graph; mean and s.e.m. are based on the actual values. **g**, Sleep in flies carrying an *R23E10-GAL4*-driven Marf overexpression construct not included in **a** and Fig. 4b ($P \geq 0.1252$, Dunn's test after Kruskal-Wallis ANOVA). Data are means ± s.e.m.; *n*, number of flies; asterisks, significant differences ($P < 0.05$) from both parental controls. For statistical details see Supplementary Table 2.

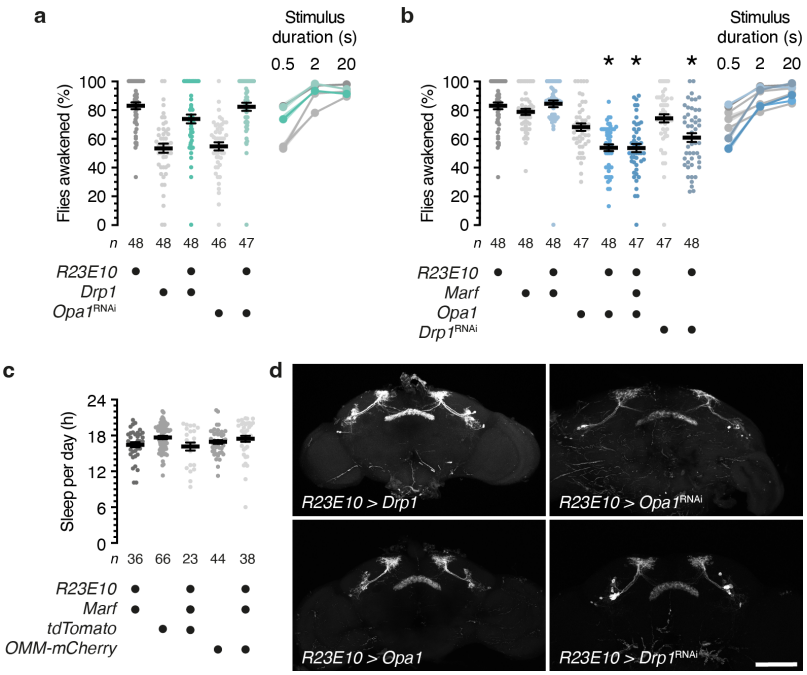

Fig. S 9 | Inducing mitochondrial fission or fusion in dFBNs alters arousal thresholds without causing overexpression artefacts or anatomical defects.

a, **b**, Percentages of flies awakened by mechanical stimuli lasting 0.5 s (left panels), 2 s, or 20 s (right panels). The average percentages awakened by 0.5-s stimuli in the left panels are reproduced on the right. Manipulations that increase fission fail to lower the arousal threshold, possibly because of a floor effect linked to the *R23E10-GAL4* strain (**a**, $P \geq 0.3354$ relative to ≥1 parental control, Dunn's test after Kruskal-Wallis ANOVA). With the exception of the overexpression of Marf alone ($P > 0.9999$), manipulations that increase fusion raise the arousal threshold (**b**, $P \leq 0.0371$, Dunn's test after Kruskal-Wallis ANOVA). **c**, Sleep in flies expressing *R23E10-GAL4*-driven Marf is insensitive to the co-expression of fluorescent proteins in the cytoplasm (tdTomato) or the outer mitochondrial membrane (OMM-mCherry) ($P \geq 0.1106$, Dunn's test after Kruskal-Wallis ANOVA), in contrast to the synergistic effect of overexpressing Opa1 (Fig. 4b, Fig. S 8a). **d**, Maximum-intensity projections of dFBNs in flies carrying *R23E10-GAL4*-driven overexpression constructs or RNAi transgenes targeting the mitochondrial fission or fusion machinery. Scale bar, 100 µm. Data are means ± s.e.m.; *n*, number of flies; asterisks, significant differences ($P < 0.05$) from both parental controls. For statistical details see Supplementary Table 2.

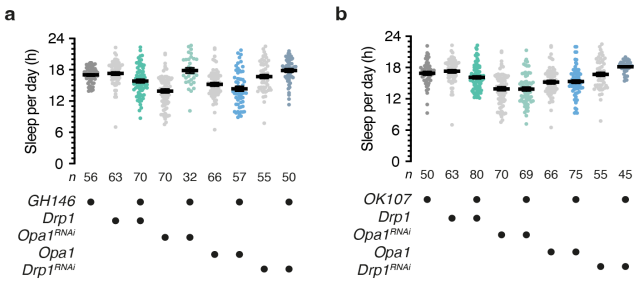

Fig. S 10 | Inducing mitochondrial fission or fusion in PNs or KCs has no consequence for sleep.

a, Sleep in flies carrying *GH146-GAL4*-driven overexpression constructs or RNAi transgenes targeting the mitochondrial fission or fusion machinery in PNs ($P \geq 0.0842$ relative to ≥1 parental control, Holm-Šídák test after ANOVA). **b**, Sleep in flies carrying *OK107-GAL4*-driven overexpression constructs or RNAi transgenes targeting the mitochondrial fission or fusion machinery in KCs ($P \geq 0.0660$ relative to ≥1 parental control, Holm-Šídák test after ANOVA). Data are means ± s.e.m.; *n*, number of flies. For statistical details see Supplementary Table 2.

Supplementary Table 1. Statistical analyses of Figures 2–4.

Figure	Statistical test	Pairwise comparison	Test statistic	*P*
2b	Two-sided Mann-Whitney test	Rested vs. sleep-deprived	U = 141	<0.0001
2c	Two-sided Mann-Whitney test	Rested vs. sleep-deprived	U = 218	0.0003
2d	Two-sided paired *t-test*	Before vs. after	t_7 = 3.192	0.0152
2e	Unpaired *t-test*	*R23E10>iATPSnFr* vs. *R23E10>iATPSnFr; CsChrimson*	t_{16} = 3.054	0.0076
2f	One-way ANOVA			
	Genotype		$F_{4,332}$ = 8.486	<0.0001
	Holm-Šidák test	*R23E10 ∩ VGlut-GAL4>Ucp4A* vs. *R23E10 ∩ VGlut-GAL4*	t_{332} = 2.501	0.0381
	Holm-Šidák test	*R23E10 ∩ VGlut-GAL4>Ucp4A* vs. *Ucp4A*	t_{332} = 5.024	<0.0001
	Holm-Šidák test	*R23E10 ∩ VGlut-GAL4>Ucp4C* vs. *R23E10 ∩ VGlut-GAL4*	t_{332} = 2.366	0.0381
	Holm-Šidák test	*R23E10 ∩ VGlut-GAL4>Ucp4C* vs. *Ucp4C*	t_{332} = 2.407	0.0381
2g	Kruskal-Wallis ANOVA			
	Experimental group		H_4 = 16.75	0.0008
	Dunn's test	*R23E10 ∩ VGlut-GAL4>mito-dR* (+ ret) vs. *R23E10 ∩ VGlut-GAL4>mito-dR* (- ret.)	Z = 3.687	0.0007
	Dunn's test	*R23E10 ∩ VGlut-GAL4>mito-dR* (+ retinal) vs. *mito-dR* (+ retinal)	Z = 3.404	0.0020
	Dunn's test	*R23E10 ∩ VGlut-GAL4>mito-dR* (+ retinal) vs. *R23E10 ∩ VGlut-GAL4* (+ retinal)	Z = 2.447	0.0432
2h	Mixed-effects model			
	Time		$F_{(2.920,777.1)}$ = 385.3	<0.0001
	Δp photogeneration		$F_{(3,268)}$ = 9.604	<0.0001
	Time x Δp photogeneration		$F_{(69,6121)}$ = 23.02	<0.0001
3b	Number of mitochondria			
	One-way ANOVA			
	Effect of SD, recovery		$F_{(2,140)}$ = 12.65	<0.0001
	Holm-Šidák test	Rested vs. sleep-deprived	t_{140} = 4.533	<0.0001
	Holm-Šidák test	Rested vs. recovered	t_{140} = 1.429	0.1551
	Two-sided unpaired *t-test*	Rested + AOX vs. sleep-deprived + AOX	t_{32}=1.235	0.2257
	Two-sided unpaired *t-test*	Rested + TrpA1 vs. sleep-deprived + TrpA1	t_{34}=0.5197	0.6067
	Volume			
	Kruskal-Wallis ANOVA			
	Effect of SD, recovery		H_3 = 34.38	<0.0001
	Dunn's test	Rested vs. sleep-deprived	Z = 2.265	0.0470
	Dunn's test	Rested vs. recovered	Z = 2.488	0.0257
	Two-sided Mann-Whitney test	Rested + AOX vs. sleep-deprived + AOX	U = 140.5	0.8985
	Two-sided unpaired *t-test*	Rested + TrpA1 vs. sleep-deprived + TrpA1	t_{34}=1.926	0.0625
	Sphericity			
	Kruskal-Wallis ANOVA			
	Effect of SD, recovery		H_3 = 46.70	<0.0001
	Dunn's test	Rested vs. sleep-deprived	Z = 2.737	0.0124
	Dunn's test	Rested vs. recovered	Z = 2.803	0.0101
	Two-sided unpaired *t-test*	Rested + AOX vs. sleep-deprived + AOX	t_{32}=0.3990	0.6925
	Two-sided unpaired *t-test*	Rested + TrpA1 vs. sleep-deprived + TrpA1	t_{34}=0.3626	0.7191
	Branch length			
	Kruskal-Wallis ANOVA			
	Effect of SD, recovery		H_3 = 47.53	<0.0001
	Dunn's test	Rested vs. sleep-deprived	Z = 3.151	0.0033
	Dunn's test	Rested vs. recovered	Z = 2.430	0.0302
	Two-sided Mann-Whitney test	Rested + AOX vs. sleep-deprived + AOX	U = 124	0.4958
	Two-sided Mann-Whitney test	Rested + TrpA1 vs. sleep-deprived + TrpA1	U = 143	0.5628
3c	Two-sided Mann-Whitney test	Rested vs. sleep-deprived	U = 11182	<0.0001
3d	Two-sided Mann-Whitney test	Rested vs. sleep-deprived	U = 449.5	<0.0001
3e	Two-sided unpaired *t-test*	Rested vs. sleep-deprived	t_{71} = 2.643	0.0101
4b	Two-way repeated-measures ANOVA			
	Time		$F_{(235,23782)}$ = 8.376	<0.0001
	Genotype		$F_{(10.86,5495)}$ = 622.2	<0.0001

	Time x Genotype		$F_{(5,506)} = 21.27$	<0.0001
4c, left	One-way ANOVA			
	Genotype (Effect of GTPases)		$F_{(9,789)} = 26.13$	<0.0001
	Holm-Šidák test	*R23E10 ∩ VGlut-GAL4>Drp1* vs. *R23E10 ∩ VGlut-GAL4*	$t_{789} = 2.340$	0.0332
	Holm-Šidák test	*R23E10 ∩ VGlut-GAL4>Drp1* vs. *Drp1*	$t_{789} = 9.126$	<0.0001
	Holm-Šidák test	*R23E10 ∩ VGlut-GAL4>Opa1^{RNAi}* vs. *R23E10 ∩ VGlut-GAL4*	$t_{789} = 6.508$	<0.0001
	Holm-Šidák test	*R23E10 ∩ VGlut-GAL4>Opa1^{RNAi}* vs. *Opa1^{RNAi}*	$t_{789} = 8.986$	<0.0001
	Holm-Šidák test	*R23E10 ∩ VGlut-GAL4>Marf,Opa1* vs. *R23E10 ∩ VGlut-GAL4*	$t_{789} = 3.809$	0.0008
	Holm-Šidák test	*R23E10 ∩ VGlut-GAL4>Marf,Opa1* vs. *Marf*	$t_{789} = 2.950$	0.0098
	Holm-Šidák test	*R23E10 ∩ VGlut-GAL4>Marf,Opa1* vs. *Opa1*	$t_{789} = 3.649$	0.0011
	Holm-Šidák test	*R23E10 ∩ VGlut-GAL4>Drp1^{RNAi}* vs. *R23E10 ∩ VGlut-GAL4*	$t_{789} = 4.741$	<0.0001
	Holm-Šidák test	*R23E10 ∩ VGlut-GAL4>Drp1^{RNAi}* vs. *Drp1^{RNAi}*	$t_{789} = 2.398$	0.0332
4c, right	Kruskal-Wallis ANOVA			
	Genotype (Effect of PA regulators)		$H_5 = 110.8$	<0.0001
	Dunn's test	*R23E10 ∩ VGlut-GAL4>zuc^{RNAi}* vs. *R23E10 ∩ VGlut-GAL4*	Z = 3.150	0.0065
	Dunn's test	*R23E10 ∩ VGlut-GAL4>zuc^{RNAi}* vs. *zuc^{RNAi}*	Z = 7.715	<0.0001
	Dunn's test	*R23E10 ∩ VGlut-GAL4>Miga^{RNAi}* vs. *R23E10 ∩ VGlut-GAL4*	Z = 2.810	0.0198
	Dunn's test	*R23E10 ∩ VGlut-GAL4>Miga^{RNAi}* vs. *Miga^{RNAi}*	Z = 6.723	<0.0001
4d, left	Two-way repeated-measures ANOVA			
	Time		$F_{(1.478,548.2)} = 2.497$	0.0992
	Genotype		$F_{(2,371)} = 8.207$	0.0003
	Time x Genotype		$F_{(94,17437)} = 6.900$	<0.0001
4d, center	Two-way repeated-measures ANOVA			
	Time		$F_{(1.487,645.2)} = 3.527$	0.0433
	Genotype		$F_{(3,434)} = 12.28$	<0.0001
	Time x Genotype		$F_{(141,20398)} = 18.01$	<0.0001
4d, right	Kruskal-Wallis ANOVA			
	Genotype		$H_6 = 78.02$	<0.0001
	Dunn's test	*R23E10 ∩ VGlut-GAL4>Opa1^{RNAi}* vs. *R23E10 ∩ VGlut-GAL4*	Z = 2.815	0.0244
	Dunn's test	*R23E10 ∩ VGlut-GAL4>Opa1^{RNAi}* vs. *Opa1^{RNAi}*	Z = 4.696	<0.0001
	Dunn's test	*R23E10 ∩ VGlut-GAL4>Marf,Opa1* vs. *R23E10 ∩ VGlut-GAL4*	Z = 2.612	0.0450
	Dunn's test	*R23E10 ∩ VGlut-GAL4>Marf,Opa1* vs. *Marf*	Z = 7.079	<0.0001
	Dunn's test	*R23E10 ∩ VGlut-GAL4>Marf,Opa1* vs. *Opa1*	Z = 4.396	<0.0001
4f	Mixed-effects model			
	Time		$F_{1.856, 114.6} = 227.5$	<0.0001
	Genotype		$F_{2, 69} = 15.56$	<0.0001
	Time x Genotype		$F_{42, 1297} = 5.822$	<0.0001
4g	Kruskal-Wallis ANOVA			
	Genotype		$H_3 = 1.465$	0.4806
	Dunn's test	*R23E10>mCD8:GFP* vs. *R23E10>Drp1*	Z = 0.8508	>0.9999
	Dunn's test	*R23E10>mCD8:GFP* vs. *R23E10>Marf,Opa1*	Z = 1.159	0.7392
	Dunn's test	*R23E10>Drp1* vs. *R23E10>Marf,Opa1*	Z = 0.3438	>0.9999
4h	Contingency table			
	$\chi2$ test		$\chi^2_2 = 7.451$	0.0241
	Standardized residuals	*R23E10>mCD8:GFP* non-bursting	+ 0.62	
		R23E10>mCD8:GFP bursting	- 1.16	
		R23E10>Drp1;mCD8:GFP non-bursting	+ 0.35	
		R23E10>Drp1;mCD8:GFP bursting	- 0.66	
		R23E10>Marf,Opa1;mCD8:GFP non-bursting	- 1.07	
		R23E10>Marf,Opa1;mCD8:GFP bursting	+ 2.01	

Supplementary Table 2. Statistical analyses of Extended Data Figures 4–10.

Figure S	Statistical test	Pairwise comparison	Test statistic	*P*
4b	Two-sided unpaired *t-test*	Rested vs. sleep-deprived	$t_{43} = 0.4407$	0.6616
4c	Kruskal-Wallis ANOVA			
	Genotype		$H_5 = 42.82$	<0.0001
	Dunn's test	*R23E10>Ucp4A* vs. *R23E10*	Z = 2.923	0.0139
	Dunn's test	*R23E10>Ucp4A* vs. *Ucp4A*	Z = 3.685	0.0009
	Dunn's test	*R23E10>Ucp4C* vs. *R23E10*	Z = 3.852	0.0005
	Dunn's test	*R23E10>Ucp4C* vs. *Ucp4C*	Z = 5.217	<0.0001
4d	Two-way repeated-measures ANOVA			
	Time		$F_{(85.36,25439)} = 1.886$	<0.0001
	Genotype		$F_{(1,298)} = 23.15$	<0.0001
	Time x genotype		$F_{(291,86718)} = 2.507$	<0.0001
4e	Kruskal-Wallis ANOVA			
	Experimental group		$H_4 = 17.92$	0.0005
	Dunn's test	*R23E10>mito-dR* (+ retinal) vs. *R23E10>mito-dR* (- retinal)	Z = 2.930	0.0102
	Dunn's test	*R23E10>mito-dR* (+ retinal) vs. *R23E10* (+ retinal)	Z = 2.600	0.0279
	Dunn's test	*R23E10>mito-dR* (+ retinal) vs. *mito-dR* (+ retinal)	Z = 4.002	0.0002
4f	Mixed-effects model			
	Time		$F_{3.346,502.9} = 267.9$	<0.0001
	Δp photogeneration		$F_{3,152} = 13.79$	<0.0001
	Time x Δp photogeneration		$F_{69, 3457} = 15.95$	<0.0001
5d	Number of mitochondria			
	Two-sided unpaired *t-test*	*TH>TrpA;R23E10>mito-GFP* vs. *R23E10>mito-GFP*	$t_{22} = 1.381$	0.1812
	Volume			
	Two-sided unpaired *t-test*	*TH>TrpA;R23E10>mito-GFP* vs. *R23E10>mito-GFP*	$t_{22} = 3.780$	0.0010
	Sphericity			
	Two-sided unpaired *t-test*	*TH>TrpA;R23E10>mito-GFP* vs. *R23E10>mito-GFP*	$t_{22} = 2.527$	0.0192
	Branch length			
	Two-sided unpaired *t-test*	*TH>TrpA;R23E10>mito-GFP* vs. *R23E10>mito-GFP*	$t_{22} = 1.317$	0.2013
5f	Number of mitochondria			
	Kruskal-Wallis ANOVA			
	Effect of SD, recovery		$H_3 = 49.88$	<0.0001
	Dunn's test	Rested vs. sleep-deprived	Z = 0.0303	>0.9999
	Dunn's test	Rested vs. recovered	Z = 6.311	<0.0001
	Two-sided unpaired *t-test*	Rested + AOX vs. sleep-deprived + AOX	$t_{35} = 2.008$	0.0524
	Two-sided unpaired *t-test*	Rested + TrpA1 vs. sleep-deprived + TrpA1	$t_{52} = 1.530$	0.1322
	Volume			
	One-way ANOVA			
	Effect of SD, recovery		$F_{(2,98)} = 61.53$	<0.0001
	Holm-Šidák test	Rested vs. sleep-deprived	$t_{98} = 3.106$	0.0025
	Holm-Šidák test	Rested vs. recovered	$t_{98} = 8.152$	<0.0001
	Two-sided unpaired *t-test*	Rested + AOX vs. sleep-deprived + AOX	$t_{35} = 1.466$	0.1515
	Two-sided Mann-Whitney test	Rested + TrpA1 vs. sleep-deprived + TrpA1	U = 240.5	0.3212
	Sphericity			
	One-way ANOVA			
	Effect of SD, recovery		$F_{(2,98)} = 37.53$	<0.0001
	Holm-Šidák test	Rested vs. sleep-deprived	$t_{98} = 3.952$	0.0001
	Holm-Šidák test	Rested vs. recovered	$t_{98} = 5.144$	<0.0001
	Two-sided unpaired *t-test*	Rested + AOX vs. sleep-deprived + AOX	$t_{35} = 1.353$	0.1848
	Two-sided unpaired *t-test*	Rested + TrpA1 vs. sleep-deprived + TrpA1	$t_{52} = 1.297$	0.2002
	Branch length			
	One-way ANOVA			
	Effect of SD, recovery		$F_{(2,98)} = 40.23$	<0.0001
	Holm-Šidák test	Rested vs. sleep-deprived	$t_{98} = 2.067$	0.0414
	Holm-Šidák test	Rested vs. recovered	$t_{98} = 6.895$	<0.0001
	Two-sided Mann-Whitney test	Rested + AOX vs. sleep-deprived + AOX	U = 136.5	0.3868
	Two-sided Mann-Whitney test	Rested + TrpA1 vs. sleep-deprived + TrpA1	U = 229.5	0.2282

5h	One-way ANOVA Genotype Holm-Šidák test Holm-Šidák test Holm-Šidák test	 *R23E10>SPLICS* vs. *R23E10>OMM-mCherry* *R23E10>SPLICS* vs. *R23E10>tdTomato-Sec61β* *R23E10>SPLICS* vs. *R23E10>CD4-tdTomato*	 $F_{(3,188)} = 2.452$ $t_{188} = 2.223$ $t_{188} = 0.1674$ $t_{188} = 1.081$	 0.0648 0.0800 0.8673 0.4829
6b	Number of mitochondria Two-sided unpaired *t-test*	Rested vs. sleep-deprived	$t_{24} = 0.3794$	0.7077
	Volume Two-sided unpaired *t-test*	Rested vs. sleep-deprived	$t_{24} = 0.2465$	0.8074
	Sphericity Two-sided unpaired *t-test*	Rested vs. sleep-deprived	$t_{24} = 0.4596$	0.6500
	Branch length Two-sided unpaired *t-test*	Rested vs. sleep-deprived	$t_{24} = 0.6332$	0.5326
6d	Number of mitochondria Two-sided Mann-Whitney test	Rested vs. sleep-deprived	U = 65	0.2534
	Volume Two-sided Mann-Whitney test	Rested vs. sleep-deprived	U = 83	0.7637
	Sphericity Two-sided Mann-Whitney test	Rested vs. sleep-deprived	U = 62	0.1953
	Branch length Two-sided unpaired *t-test*	Rested vs. sleep-deprived	$t_{27} = 0.3933$	0.6972
7b	Volume One-way ANOVA Genotype Holm-Šidák test Holm-Šidák test Holm-Šidák test Holm-Šidák test	 *R23E10>mito-GFP;Drp1* vs. *R23E10>mito-GFP;Marf,Opa1* *R23E10>mito-GFP;Drp1* vs. *R23E10>mito-GFP;Drp1^{RNAi}* *R23E10>mito-GFP;Opa1^{RNAi}* vs. *R23E10>mito-GFP;Marf,Opa1* *R23E10>mito-GFP;Opa1^{RNAi}* vs. *R23E10>mito-GFP;Drp1^{RNAi}*	 $F_{(3,47)} = 9.995$ $t_{47} = 2.137$ $t_{47} = 2.327$ $t_{47} = 4.528$ $t_{47} = 4.539$	 <0.0001 0.0480 0.0480 0.0002 0.0002
	Sphericity One-way ANOVA Genotype Holm-Šidák test Holm-Šidák test Holm-Šidák test Holm-Šidák test	 *R23E10>mito-GFP;Drp1* vs. *R23E10>mito-GFP;Marf,Opa1* *R23E10>mito-GFP;Drp1* vs. *R23E10>mito-GFP;Drp1^{RNAi}* *R23E10>mito-GFP;Opa1^{RNAi}* vs. *R23E10>mito-GFP;Marf,Opa1* *R23E10>mito-GFP;Opa1^{RNAi}* vs. *R23E10>mito-GFP;Drp1^{RNAi}*	 $F_{(3,47)} = 5.476$ $t_{47} = 2.178$ $t_{47} = 2.501$ $t_{47} = 3.032$ $t_{47} = 3.311$	 0.0026 0.0344 0.0316 0.0118 0.0071
	Branch length One-way ANOVA Genotype Holm-Šidák test Holm-Šidák test Holm-Šidák test Holm-Šidák test	 *R23E10>mito-GFP;Drp1* vs. *R23E10>mito-GFP;Marf,Opa1* *R23E10>mito-GFP;Drp1* vs. *R23E10>mito-GFP;Drp1^{RNAi}* *R23E10>mito-GFP;Opa1^{RNAi}* vs. *R23E10>mito-GFP;Marf,Opa1* *R23E10>mito-GFP;Opa1^{RNAi}* vs. *R23E10>mito-GFP;Drp1^{RNAi}*	 $F_{(3,47)} = 7.148$ $t_{47} = 2.202$ $t_{47} = 2.956$ $t_{47} = 3.247$ $t_{47} = 4.001$	 0.0005 0.0326 0.0097 0.0064 0.0009
7c	Volume Kruskal-Wallis ANOVA Genotype Dunn's test Dunn's test Dunn's test Dunn's test	 *R23E10>mito-GFP;Drp1* vs. *R23E10>mito-GFP;Marf,Opa1* *R23E10>mito-GFP;Drp1* vs. *R23E10>mito-GFP;Drp1^{RNAi}* *R23E10>mito-GFP;Opa1^{RNAi}* vs. *R23E10>mito-GFP;Marf,Opa1* *R23E10>mito-GFP;Opa1^{RNAi}* vs. *R23E10>mito-GFP;Drp1^{RNAi}*	 $H_4 = 80.92$ Z = 3.166 Z = 7.026 Z = 4.152 Z = 7.903	 <0.0001 0.0062 <0.0001 0.0001 <0.0001
	Sphericity One-way ANOVA Genotype Holm-Šidák test Holm-Šidák test Holm-Šidák test Holm-Šidák test	 *R23E10>mito-GFP;Drp1* vs. *R23E10>mito-GFP;Marf,Opa1* *R23E10>mito-GFP;Drp1* vs. *R23E10>mito-GFP;Drp1^{RNAi}* *R23E10>mito-GFP;Opa1^{RNAi}* vs. *R23E10>mito-GFP;Marf,Opa1* *R23E10>mito-GFP;Opa1^{RNAi}* vs. *R23E10>mito-GFP;Drp1^{RNAi}*	 $F_{(3,120)} = 8.747$ $t_{120} = 2.421$ $t_{120} = 3.001$ $t_{120} = 3.635$ $t_{120} = 4.512$	 <0.0001 0.0170 0.0065 0.0012 <0.0001
	Branch length Kruskal-Wallis ANOVA Genotype Dunn's test Dunn's test Dunn's test Dunn's test	 *R23E10>mito-GFP;Drp1* vs. *R23E10>mito-GFP;Marf,Opa1* *R23E10>mito-GFP;Drp1* vs. *R23E10>mito-GFP;Drp1^{RNAi}* *R23E10>mito-GFP;Opa1^{RNAi}* vs. *R23E10>mito-GFP;Marf,Opa1* *R23E10>mito-GFP;Opa1^{RNAi}* vs. *R23E10>mito-GFP;Drp1^{RNAi}*	 $H_4 = 24.68$ Z = 1.890 Z = 2.553 Z = 3.491 Z = 4.590	 <0.0001 0.2350 0.0427 0.0019 <0.0001
7d	Two-way ANOVA			

	Drp1		$F_{1,118}$ = 29.05	<0.0001
	Sleep history		$F_{1,118}$ = 22.82	<0.0001
	Drp1 x sleep history		$F_{1,118}$ = 2.576	0.1112
8a	One-way ANOVA			
	Genotype (Effect of GTPases)		$F_{11,714}$ = 33.80	<0.0001
	Holm-Šidák test	*R23E10>Drp1* vs. *R23E10*	t_{714} = 3.170	0.0079
	Holm-Šidák test	*R23E10>Drp1* vs. *Drp1*	t_{714} = 4.332	0.0001
	Holm-Šidák test	*R23E10>Opa1^{RNAi}* vs. *R23E10*	t_{714} = 7.729	<0.0001
	Holm-Šidák test	*R23E10>Opa1^{RNAi}* vs. *Opa1^{RNAi}*	t_{714} = 6.219	<0.0001
	Holm-Šidák test	*R23E10>Marf* vs. *R23E10*	t_{714} = 0.1551	0.8768
	Holm-Šidák test	*R23E10>Marf* vs. *Marf*	t_{714} = 1.726	0.1622
	Holm-Šidák test	*R23E10>Opa1* vs. *R23E10*	t_{714} = 2.963	0.0115
	Holm-Šidák test	*R23E10>Opa1* vs. *Opa1*	t_{714} = 4.505	<0.0001
	Holm-Šidák test	*R23E10>Opa1,Marf* vs. *R23E10*	t_{714} = 6.398	<0.0001
	Holm-Šidák test	*R23E10>Opa1,Marf* vs. *Opa1*	t_{714} = 7.802	<0.0001
	Holm-Šidák test	*R23E10>Opa1,Marf* vs. *Marf*	t_{714} = 7.301	<0.0001
	Holm-Šidák test	*R23E10>Drp1^{RNAi}* vs. *R23E10*	t_{714} = 8.503	<0.0001
	Holm-Šidák test	*R23E10>Drp1^{RNAi}* vs. *Drp1^{RNAi}*	t_{714} = 2.990	0.0115
8b	Kruskal-Wallis ANOVA			
	Genotype		H_7 = 94.10	<0.0001
	Dunn's test	*R23E10>zuc^{RNAi}* vs. *R23E10*	Z = 2.729	0.0381
	Dunn's test	*R23E10>zuc^{RNAi}* vs. *zuc^{RNAi}*	Z = 4.610	<0.0001
	Dunn's test	*R23E10>Miga$^{RNAi\ 110737KK}$* vs. *R23E10*	Z = 4.876	<0.0001
	Dunn's test	*R23E10>Miga$^{RNAi\ 110737KK}$* vs. *Miga$^{RNAi\ 110737KK}$*	Z = 3.615	0.0018
	Dunn's test	*R23E10>Miga^{RNAi}* vs. *R23E10*	Z = 6.911	<0.0001
	Dunn's test	*R23E10>Miga^{RNAi}* vs. *Miga$^{RNAi\ 5492GD}$*	Z = 4.722	<0.0001
8c	Kruskal-Wallis ANOVA			
	Genotype		H_5 = 78.08	<0.0001
	Dunn's test	*R23E10>Drp1-HA* vs. *R23E10*	Z = 6.175	<0.0001
	Dunn's test	*R23E10>Drp1-HA* vs. *Drp1-HA*	Z = 2.793	0.0209
	Dunn's test	*R23E10>Drp1$^{Feany\ lab}$* vs. *R23E10*	Z = 7.861	<0.0001
	Dunn's test	*R23E10>Drp1$^{Feany\ lab}$* vs. *Drp1$^{Feany\ lab}$*	Z = 4.875	<0.0001
8d	One-way ANOVA			
	Genotype		$F_{12,759}$ = 29.05	<0.0001
	Holm-Šidák test	*R23E10>Opa1^{shRNA330266SH}* vs. *R23E10*	t_{759} = 2.583	0.0199
	Holm-Šidák test	*R23E10>Opa1^{shRNA330266SH}* vs. *Opa1^{shRNA330266SH}*	t_{759} = 4.532	<0.0001
	Holm-Šidák test	*R23E10>Opa1$^{RNAi\ \#32358}$* vs. *R23E10*	t_{759} = 3.592	0.0014
	Holm-Šidák test	*R23E10>Opa1$^{RNAi\ \#32358}$* vs. *UAS-Opa1$^{RNAi\ \#32358}$*	t_{759} = 7.650	<0.0001
	Holm-Šidák test	*R23E10>Opa1$^{miRNA.CDS}$* vs. *R23E10*	t_{759} = 8.277	<0.0001
	Holm-Šidák test	*R23E10>Opa1$^{miRNA.CDS}$* vs. *UAS-Opa1$^{miRNA.CDS}$*	t_{759} = 8.663	<0.0001
	Holm-Šidák test	*R23E10>smOpa1 (X)* vs. *R23E10*	t_{759} = 3.679	0.0013
	Holm-Šidák test	*R23E10>smOpa1 (X)* vs. *smOpa1 (X)*	t_{759} = 2.478	0.0199
	Holm-Šidák test	*R23E10>smOpa1 (II)* vs. *R23E10*	t_{759} = 7.777	<0.0001
	Holm-Šidák test	*R23E10>smOpa1 (II)* vs. *UAS-smOpa1 (II)*	t_{759} = 2.947	0.0099
	Holm-Šidák test	*R23E10>smOpa1 (III)* vs. *R23E10*	t_{759} = 7.495	<0.0001
	Holm-Šidák test	*R23E10>smOpa1 (III)* vs. *UAS-smOpa1 (III)*	t_{759} = 9.094	<0.0001
8e	One-way ANOVA			
	Genotype		$F_{10,643}$ = 11.60	<0.0001
	Holm-Šidák test	*R23E10>Marf$^{RNAi\ 40478GD}$* vs. *R23E10*	t_{643} = 1.901	0.2117
	Holm-Šidák test	*R23E10>Marf$^{RNAi\ 40478GD}$* vs. *Marf$^{RNAi\ 40478GD}$*	t_{643} = 2.642	0.0496
	Holm-Šidák test	*R23E10>Marf$^{RNAi\ 105261KK}$* vs. *R23E10*	t_{643} = 0.1334	0.8939
	Holm-Šidák test	*R23E10>Marf$^{RNAi\ 105261KK}$* vs. *Marf$^{RNAi\ 105261KK}$*	t_{643} = 2.310	0.1017
	Holm-Šidák test	*R23E10>Marf$^{RNAi\ \#55189}$* vs. *R23E10*	t_{643} = 1.276	0.4397
	Holm-Šidák test	*R23E10>Marf$^{RNAi\ \#55189}$* vs. *Marf$^{RNAi\ \#55189}$*	t_{643} = 5.295	<0.0001
	Holm-Šidák test	*R23E10>smMarf (II)* vs. *R23E10*	t_{643} = 4.144	0.0003
	Holm-Šidák test	*R23E10>smMarf (II)* vs. *smMarf (II)*	t_{643} = 6.863	<0.0001
	Holm-Šidák test	*R23E10>smMarf (III)* vs. *R23E10*	t_{643} = 2.733	0.0443
	Holm-Šidák test	*R23E10>smMarf (III)* vs. *smMarf (III)*	t_{643} = 1.356	0.4397
8f, left	Two-way repeated-measures ANOVA			
	Time		$F_{1.442,363.3}$ = 13.33	<0.0001
	Genotype		$F_{2,\ 252}$ = 4.247	0.0153
	Time x genotype		$F_{94,11844}$ = 6.622	<0.0001
8f, center	Two-way repeated-measures ANOVA			
	Time		$F_{1.367,\ 307.5}$ = 357.9	<0.0001
	Genotype		$F_{3,\ 225}$ = 3.296	0.0213
	Time x genotype		$F_{213,\ 15975}$ = 6.160	<0.0001
8f, right	Kruskal-Wallis ANOVA			
	Genotype		H_6 = 37.30	<0.0001
	Dunn's test	*R23E10>Opa1^{RNAi} vs. R23E10*	Z = 3.545	0.0020
	Dunn's test	*R23E10>Opa1^{RNAi} vs. Opa1^{RNAi}*	Z = 3.272	0.0053
	Dunn's test	*R23E10>Opa1,Marf vs. R23E10*	Z = 2.900	0.0186
	Dunn's test	*R23E10>Opa1,Marf vs. Marf*	Z = 4.266	<0.0001
	Dunn's test	*R23E10>Opa1,Marf vs. Opa1*	Z = 3.484	0.0025
8g	Kruskal-Wallis ANOVA			
	Genotype		H_3 = 7.932	0.0189
	Dunn's test	*R23E10>Marf-FLAG* vs. *R23E10*	Z = 1.862	0.1252
	Dunn's test	*R23E10>Marf-FLAG* vs. *Marf-FLAG*	Z = 0.8203	0.8241

9a, b	Kruskal-Wallis ANOVA			
	Genotype		H_{12} = 193.4	<0.0001
	Dunn's test	*R23E10>Drp1* vs. *R23E10*	Z = 2.229	0.3354
	Dunn's test	*R23E10>Drp1* vs. *Drp1*	Z = 4.528	<0.0001
	Dunn's test	*R23E10>Opa1^{RNAi}* vs. *R23E10*	Z = 0.04653	>0.9999
	Dunn's test	*R23E10>Opa1^{RNAi}* vs. *Opa1^{RNAi}*	Z = 6.468	<0.0001
	Dunn's test	*R23E10>Marf* vs. *R23E10*	Z = 0.6387	>0.9999
	Dunn's test	*R23E10>Marf* vs. *Marf*	Z = 1.700	>0.9999
	Dunn's test	*R23E10>Opa1* vs. *R23E10*	Z = 6.977	<0.0001
	Dunn's test	*R23E10>Opa1* vs. *Opa1*	Z = 3.132	0.0226
	Dunn's test	*R23E10>Marf,Opa1* vs. *R23E10*	Z = 6.806	<0.0001
	Dunn's test	*R23E10>Marf,Opa1* vs. *Marf*	Z = 5.751	<0.0001
	Dunn's test	*R23E10>Marf,Opa1* vs. *Opa1*	Z = 2.983	0.0371
	Dunn's test	*R23E10>Drp1^{RNAi}* vs. *R23E10*	Z = 5.139	<0.0001
	Dunn's test	*R23E10>Drp1^{RNAi}* vs. *Drp1^{RNAi}*	Z = 3.213	0.0170
9c	Kruskal-Wallis ANOVA			
	Genotype		H_5 = 9.949	0.0413
	Dunn's test	*R23E10>Marf,tdTomato* vs. *R23E10>Marf*	Z = 0.08112	>0.9999
	Dunn's test	*R23E10>Marf,tdTomato* vs. *tdTomato*	Z = 1.796	0.2899
	Dunn's test	*R23E10>Marf,OMM-mCherry* vs. *R23E10>Marf*	Z = 2.202	0.1106
	Dunn's test	*R23E10>Marf,OMM-mCherry* vs. *OMM-mCherry*	Z = 1.898	0.2310
10a	One-way ANOVA			
	Genotype		$F_{8,510}$= 16.13	<0.0001
	Holm-Šidák test	*GH146>Drp1* vs. *GH146*	t_{510} = 2.385	0.0842
	Holm-Šidák test	*GH146>Drp1* vs. *Drp1*	t_{510} = 3.031	0.0153
	Holm-Šidák test	*GH146>Opa1^{RNAi}* vs. *GH146*	t_{510} = 1.393	0.2211
	Holm-Šidák test	*GH146>Opa1^{RNAi}* vs. *Opa1^{RNAi}*	t_{510} = 6.731	<0.0001
	Holm-Šidák test	*GH146>Opa1* vs. *GH146*	t_{510} = 5.143	<0.0001
	Holm-Šidák test	*GH146>Opa1* vs. *Opa1*	t_{510} = 1.755	0.2211
	Holm-Šidák test	*GH146>Drp1^{RNAi}* vs. *GH146*	t_{510} = 1.609	0.2211
	Holm-Šidák test	*GH146>Drp1^{RNAi}* vs. *Drp1^{RNAi}*	t_{510} = 2.162	0.1187
10b	One-way ANOVA			
	Genotype		$F_{8,564}$ = 19.13	<0.0001
	Holm-Šidák test	*OK107>Drp1* vs. *OK107*	t_{564} = 1.638	0.2757
	Holm-Šidák test	*OK107>Drp1* vs. *Drp1*	t_{564} = 2.632	0.0429
	Holm-Šidák test	*OK107>Opa1^{RNAi}* vs. *OK107*	t_{564} = 6.202	<0.0001
	Holm-Šidák test	*OK107>Opa1^{RNAi}* vs. *Opa1^{RNAi}*	t_{564} = 0.09364	0.9764
	Holm-Šidák test	*OK107>Opa1* vs. *OK107*	t_{564} = 3.307	0.0070
	Holm-Šidák test	*OK107>Opa1* vs. *Opa1*	t_{564} = 0.1937	0.9764
	Holm-Šidák test	*OK107>Drp1^{RNAi}* vs. *OK107*	t_{564} = 2.396	0.0660
	Holm-Šidák test	*OK107>Drp1^{RNAi}* vs. *Drp1^{RNAi}*	t_{564} = 2.797	0.0316